Available online at www.sciencedirect.com
SCIENCE DIRECT®
Journal of Computational Physics 206 (2005) 727–780
JOURNAL OF COMPUTATIONAL PHYSICS
www.elsevier.com/locate/jcp

Local spectral time splitting method for first- and second-order partial differential equations

Sining Yu [a], Shan Zhao [a], G.W. Wei [a,b,*]

[a] Department of Mathematics, Michigan State University, East Lansing, MI 48824, USA
[b] Department of Electrical and Computer Engineering, Michigan State University, East Lansing, MI 48824, USA

Received 13 October 2004; received in revised form 4 January 2005; accepted 10 January 2005
Available online 3 March 2005

This paper is dedicated to Professor David Gottlieb on the occasion of his 60th birthday

Abstract

A family of local spectral evolution kernels (LSEKs) are derived for analytically integrating a class of partial differential equations (PDEs)

$$\frac{\partial}{\partial t}u = \left[A(t)\frac{\partial^2}{\partial x^2} + B(t)\frac{\partial}{\partial x} + C(t)\right]u.$$

The LSEK can solve the above PDEs with x-independent coefficients in a single step. They are utilized in operator splitting schemes to arrive at a local spectral time-splitting (LSTS) method for solving more general linear and/or nonlinear PDEs. Like previous local spectral methods, this new method is of controllable accuracy in both spatial and temporal discretizations, and it can be of spectral accuracy in space and arbitrarily high-order accuracy in time. Its complexity scales as O(N) at a fixed level of accuracy. It is explicit, time transverse invariant, unconditionally stable for many problems whose two split parts are both analytically integrable. It adopts uniform grid meshes. The proposed method is extensively validated in terms of accuracy, stability, efficiency, robustness and reliability by the Fokker–Planck equation, the Black–Scholes equation, the heat equation, the plane wave propagation, the Zakharov system, and a linear harmonic oscillator. Numerical applications are considered to Fisher's equation, the generalized nonlinear Schrödinger equation, the Bose–Einstein condensates, and the Schrödinger equation in the semi-classical regime. Numerical results compare well with those in the literature.

Keywords: Local spectral method; Discrete singular convolution; Wavelet collocation; Split step

* Corresponding author. Tel.: +1 517 353 4689.
E-mail address: wei@math.msu.edu (G.W. Wei).

0021-9991/$ - see front matter © 2005 Elsevier Inc. All rights reserved.
doi:10.1016/j.jcp.2005.01.010

1. Introduction

Most real world problems are of multi-physics, multi-component and multi-time scale in nature. Dynamics of such problems are often governed by nonlinear partial differential equations (PDEs) that do not admit analytical solutions. Numerical simulations of these problems are indispensable and challenging. A fully coupled implicit scheme which yields to the resolution of strongly nonlinear systems would be the most desirable approach. It is, however, often out of reach due to the required large computer memory and CPU time. Consequently, alternative approaches are necessary. One approach is to adopt semi-implicit and even explicit schemes. However, a wide range of time scales induce the stiffness in time integration. A typical case is a reaction, diffusion, and convection system where the slowest process determines the time step and the stability of the time integration. In such cases, schemes based on error estimates and local time adaptation are used. Another possible approach is to analyze a reduced system with fewer unknowns and lower dimensional kinematics. Special care has to be paid in carrying out the reduction. However, for fully coupled problems, it is fundamental to keep the information about global coupling.

A major class of efficient alternative approaches are based on time splitting methods, also called operator splitting or fractional step methods [1–3]. Most natural splitting schemes are frequently constructed according to either physical components and subsystems, such as density, velocity, energy and pressure, or physical processes, such as reaction, diffusion and convection, or dimension, such as in the alternating direction implicit method [4]. Sometimes, these splitting methods might be associated with semi-Lagrangian or Eulerian–Lagrangian methods [1] as the advection equation is solved by along a characteristic path. These splitting algorithms may suffer from two main disadvantages [5,6]: splitting error in the composite algorithm and determination of boundary conditions for the split equations. Intermediate boundary conditions are exploited for the split equations [7,8]. Splitting errors of time splitting methods have been analyzed by a number of researchers [9–11]. For an operator equation of the form

$$\frac{\partial}{\partial t}u = (L_1 + L_2)u,$$

most widely used time splitting schemes are the Lie formulae

$$\exp(L_1 t)\exp(L_2 t), \exp(L_2 t)\exp(L_1 t)$$

and the Strang formulae [12]

$$\exp(L_1 t/2)\exp(L_2 t)\exp(L_1 t/2), \exp(L_2 t/2)\exp(L_1 t)\exp(L_2 t/2).$$

There will be no splitting error if operators L_1 and L_2 are commutable. High-order time-splitting schemes [13] can be constructed to reduced splitting errors in the Lie and the Strang formulae.

Some time splitting methods are designed under geometric consideration. For example, symplectic algorithms are constructed to preserve Poincaré invariants of classical Hamiltonian systems in long time integration. Time splitting methods are frequently employed as a means to attain higher order symplectic algorithms [14–17]. These methods are crucial to nonlinear integrable systems such as the sine-Gordon equation and the nonlinear Schrödinger equation that admit homoclinic orbits in their phase space geometry, which poses a severe challenge to their numerical integration [18–20]. Ablowitz et al. [19] have argued that being symplectic alone is not sufficient to guarantee the correctness of the solution and the preservation of the invariants. Numerically induced chaos can be produced by some symplectic algorithms for completely integrable systems when the initial value is chosen close to a homoclinic orbit. High-order discretization in both space and time are particularly important. Many high-order symplectic time-splitting schemes have been proposed [15–17]. For example, Forest and Ruth [15] have constructed a fourth-order time-splitting method to better preserve the Poincaré invariants. A systematic procedure was proposed by Yoshida [16] for attaining arbitrarily high even order time-splitting methods.

Many other time splitting methods are designed to take the advantage of operator diagonalization. For example, the time evolution equation for the wavevector $\mathsf{W}(\mathbf{x}, t)$ of a quantum particle

$$\mathrm{i}\hbar\frac{\partial}{\partial t}\mathsf{W} = -\frac{\hbar^2}{2m}\frac{\partial^2}{\partial \mathbf{x}^2}\mathsf{W} + V(\mathbf{x})\mathsf{W}$$

can be split according to the kinetic energy operator (i.e., $L_1 = -(\hbar^2/2m)(\partial^2/\partial\mathbf{x}^2)$, where $\hbar$ is the Planck constant divided by 2π and m is the mass of the particle), and the potential energy operator $L_2 = V(\mathbf{x})$. The kinetic energy operator is diagonal in the momentum representation (or basis), which can be treated by the Fourier collocation method, while its potential energy operator is diagonal in the position representation, which can be realized by on-grid interpolations. Consequently, a time splitting between these two non-commutable operators leads to an explicit numerical method that is unconditionally stable. In fact, the magic of unconditionally stable can be achieved for any split system whose all subsystems are *analytically* integrable. For many PDEs, the key for success is to integrate the time evolution equation involving spatial derivatives analytically so as to bypass the Courant–Friedrich–Lewy (CFL) constraint. This can be conventionally done by using the Fourier pseudospectral (FP) method, i.e., the Fourier collocation method. The resulting scheme is called Fourier pseudospectral time splitting (FPTS) method [21,22]. The FPTS has found its success in solving the complex Ginzburg–Landau equation [23], the Schrödinger equation [21,24,25], the Korteweg–de Vries (KdV) equation [26–28] and three-dimensional (3D) Maxwell's equations [29]. Recently, Bao, Jin and their collaborators have successfully applied the FPTS method for the Zakharov system [31], Bose–Einstein condensation [32,33] and the Schrödinger equation in the semiclassical regime [34]. The FPTS is very efficient, powerful and attractive because of its spectral accuracy in space and unconditional stability in time. However, the FPTS is based on the Fourier pseudospectral method that is restricted to periodic boundary conditions and simple geometries. As such, it cannot be applied to many realistic problems. For other simple boundary conditions, such as Dirichlet, Neumann and unbound boundary conditions, Chebyshev, Legendre, Laguerre or Hermite polynomial may be used to construct spectral bases for the time evolution equation [32,35,36]. Lazaridis et al. [35] constructed a time-splitting Gauss–Hermite algorithm for fast and accurate simulation of soliton propagation by using chirped Gauss–Hermite functions. Kremp et al. [36] proposed an interesting time-splitting Gauss–Hermite collocation method for solving the nonlinear Schrödinger equation. The efficiency of these methods was compared with the FPTS. Common features of global spectral bases are that they are of spectral accuracy and extremely high efficiency whenever applicable, but have limited flexibility in handling complex and/or mixed boundary conditions.

In general, spectral methods are global in nature, which means that they approximate a function and/or its derivatives at a point by using the information at all the points in the domain [37–47]. Consequently, they have full matrices and their approximation errors for analytical functions decay exponentially with respect to the increase in the number of grid points N [44–46]. With the aid of the fast Fourier transform (FFT) technique, the number of operations for the Fourier spectral method scales as $O(N\log N)$ for differentiation. Indeed, they are some of the most efficient and powerful methods for scientific and engineering computations whenever they are applicable [37–47]. However, the major limitations of spectral methods are their lack of flexibility for different boundary conditions and complex geometry, and stability for explicit time integration due to non-uniform meshes. For example, problems with multiple complex boundary conditions arisen in structural analysis, such as plate and shell vibrations where differential equations of order 4–8 (even 12 in some cases) are frequently encountered [48], are mostly inaccessible to spectral methods in general due to their global nature. Spectral element methods are designed to overcome the problem of limited ability of spectral methods for complex geometries [49,50,43]. They work extremely well on relatively simple geometries but are not yet as robust as finite element, finite difference and finite volume methods in handling arbitrary geometries. Moreover, except for Fourier pseudospectral methods, most other spectral methods adopt non-uniform grid points, such as Laguerre–Gauss–Radau points and

Chebyshev–Gauss–Lobatto points [44]. These grid points typically produce the smallest grid spacing essentially proportional to $O(1/N^2)$, here N is the total number of grid points in a given interval, and thus induce a severe stability requirement of $\Delta t \propto (1/N^2)$ for convection and $\Delta t \propto (1/N^4)$ for diffusion. Consequently, it is impractical to use non-uniform grid spectral methods in the explicit integration of evolution PDEs. Furthermore, the matrix constructed by using global spectral methods for the solution of an elliptic differential equation is full and usually has a high condition number, which often leads to numerical instability. Much of the current research in spectral methods focuses on relieving spectral methods' limitations on boundary condition, geometry and stability.

Recently, a family of local spectral (LS) methods, also called the discrete singular convolution (DSC) [51,52], were proposed as a natural generalization of the global spectral methods to overcome the limitations of classic spectral methods, while to maintain the spectral accuracy. It provides a framework for a unified description of Galerkin, collocation and finite difference methods [53]. Since collocation schemes can be regarded as generalized finite differences, the DSC collocation has been shown to be a generalized finite difference scheme [53]. Nevertheless, it goes far beyond the standard finite difference scheme. The DSC provides a wavelet collocation approach to singular convolutions, including the distributions of the delta type $\delta^{(n)}$, using locally confined kernels. The DSC algorithm has its root in the theory of distribution and wavelet analysis. It has found its success in many applications, such as the solution of nonlinear equations [20,67,54], structural analysis [52,55–57], compressible and incompressible fluid flows [56,58–60], electromagnetic wave propagation and scattering [61–63] and image analysis [64]. The DSC is the only available numerical method for the prediction of thousands of high-frequency vibration modes in beams, plates and shells [65,66], for which other existing methods encounter numerical instability. Moreover, a DSC-based conjugate filter scheme has been shown to provide some of the best results for the interaction of shock and high frequency entropy waves [59], which is another example that other existing methods have difficulty. Indeed, the DSC algorithm has spectral methods' accuracy [54,67–69] and local methods' flexibility for complex boundary condition [52,57,65] and moderately complex geometry [58,60].

The objective of the present paper is to introduce a novel local spectral method for being used in the time splitting formulation. A family of local spectral evolution kernels (LSEKs) are constructed to analytically integrate the evolution equation of the form

$$\frac{\partial}{\partial t}u = L_1 u = \left[A(t)\frac{\partial^2}{\partial x^2} + B(t)\frac{\partial}{\partial x} + C(t)\right]u,$$

with a positive real part of A ($\mathrm{Re}(A) \geqslant 0$). Unconditionally stable local spectral time splitting (LSTS) methods can be obtained if the remaining evolution equation of the form $(\partial/\partial t)u = L_2 u$ is also analytically integrable. The LSTS is of spectral accuracy in space and can be arbitrarily high order in time when it is implemented with an appropriate high-order time-splitting scheme proposed by Yoshida [16]. The local spectral evolution kernels are constructed from Hermite functions. However, unlike standard global Hermite spectral methods [32,35], the LSEKs adopt uniform grids and have banded matrices, just like other DSC kernels. In fact, the length of the grid stencil, and thus the accuracy of the LSEK can be controlled according to the needs of the problem of interest, which is another feature of the DSC inherited from wavelet analysis. The major advantage of the present LSTS method is its ability for handling arbitrary boundary conditions and flexibility for moderately complex geometry.

This paper is organized as the follows. Section 2 is devoted to the method and algorithm of the LSTS. The LSEKs are derived and time splitting schemes are briefly reviewed. In Section 3, we investigate the accuracy, stability, computing time and parameter dependence of the LSTS. The latter is extensively validated by a comparison with the FPTS method over a number of linear and nonlinear PDEs, including the Fokker–Planck equation, the heat equation, the free plane wave propagation, the Zakharov system and a quantum harmonic oscillator. In Section 4, we apply the LSTS to the solution of Fisher's equation, the

nonlinear Schrödinger equation, the Gross–Pitaevskii equation for Bose–Einstein condensation and the Schrödinger equation in the semi-classical regime. The numerical results in this section are compared with those in the literature. This paper ends with a conclusion.

2. Theory and algorithms

In this section, the local spectral method is briefly reviewed, which serves as a basis and establishes notation for the new time splitting method. A Hermite function representation of the time evolution operator is derived. Dispersion analysis is carried out to better understand the behavior of the LSEK. High-order local spectral time-splitting (LSTS) methods are given.

2.1. Local spectral methods

Discrete singular convolution (DSC) is a general framework for constructing local spectral methods. It provides discrete approximations to the singular convolution

$$f^{(l)}(x) = \int \mathsf{d}^{(l)}(x - x')f(x')\,\mathrm{d}x' \quad (l = 0, 1, 2, \ldots), \tag{1}$$

where $\mathsf{d}(x)$ is the delta distribution. As the delta distribution does not have a value anywhere, its approximation is necessary so that it can be digitized in a computer. Approximations of both positive type and Dirichlet type are described in the literature [70,71]. Some of the approximations, such as the Shannon (sinc) kernel and the Dirichlet kernel, essentially give rise to the classic Fourier spectral methods. Some of local spectral kernels [51] are constructed by regularizing the Shannon kernel

$$\mathsf{d}_{h,\mathsf{r}}(x - x_k) = \frac{\sin\frac{\pi}{h}(x - x_k)}{\frac{\pi}{h}(x - x_k)} \exp\left[-\frac{(x - x_k)^2}{2\mathsf{r}^2}\right] \tag{2}$$

and the Dirichlet kernel

$$\mathsf{d}_{h,\mathsf{r}}(x - x_k) = \frac{\sin\left[\frac{\pi}{h}(x - x_k)\right]}{(2M' + 1)\sin\left[\frac{\pi}{h}\frac{x - x_k}{2M'+1}\right]} \exp\left[-\frac{(x - x_k)^2}{2\mathsf{r}^2}\right], \tag{3}$$

where M' is a parameter and h is the grid spacing. A regularized Lagrange kernel (RLK) [72],

$$\mathsf{d}_{h,\mathsf{r}}(x - x_k) = \prod_{i=k-M', i\neq k}^{i=k+M'} \frac{x - x_i}{x_k - x_i} \exp\left[-\frac{(x - x_k)^2}{2\mathsf{r}^2}\right], \tag{4}$$

was constructed by regularizing the classic Lagrange polynomial. However, the implementation of the RLK is entirely different from that of the classic Lagrange polynomial [46]. Many other DSC kernels are given in [51,52]. A function and its derivatives can be approximated by the DSC algorithm as

$$\begin{aligned} f^{(l)}_{M,\mathsf{r}}(x) &= \frac{\mathrm{d}^l}{\mathrm{d}x^l} \sum_{k=-M}^{M} \mathsf{d}_{h,\mathsf{r}}(x - x_k)f(x_k), \quad l = 0, 1, 2, \ldots \\ &= \sum_{k=-M}^{M} \mathsf{d}^{(l)}_{h,\mathsf{r}}(x - x_k)f(x_k), \end{aligned} \tag{5}$$

where $2M + 1$ is the length of the stencil and $\{x_k\}$ are centered around x.

The error estimation of the regularized Shannon kernel has been given by Qian [68].

Theorem 1. [68] *Let $f(x)$ be a function $f \in L^{\infty}(R) \cap L^2(R) \cap C^l(R)$ and bandlimited to B, $(B < (\pi/h))$, $l \in Z^+$, $\mathsf{r} = rh > 0$, $M \in N$, $M \geqslant (lr/\sqrt{2})$. Then*

$$\left\| f^{(l)} - f^{(l)}_{M,\mathsf{r}} \right\|_{L^{\infty}(R)} \leqslant \mathsf{b} \exp\left(-\frac{\mathsf{a}^2}{2r^2}\right), \tag{6}$$

where

$$\mathsf{a} = \min\{M, r^2(\pi - Bh)\}, \tag{7}$$

$$\mathsf{b} = \frac{\mathrm{e}^{\pi} r(l+1)!}{h^l \pi \mathsf{a}} \left(\sqrt{2B}\|f\|_{L^2(R)} + 2r\|f\|_{L^{\infty}(R)}\right).$$

Here N is the number of the grid points. The L_{∞} error given by Eq. (6) decays exponentially with respect to the increase of the DSC band width M.

Proof 1. See Ref. [68]. □

The local spectral kernels can also be constructed by using the classical polynomial approximation to the delta distribution. Korevaar [73] constructed a Hermite function approximation of the delta distribution in his classic work "Pansions and the theory of Fourier transforms". Independently, Hoffman et al. [74] derived the approximation and an expression for its arbitrary derivatives. Let us define the Hermite function as

$$h_n(x) = \exp(-x^2) H_n(x),$$

where $H_n(x)$ is the classic Hermite polynomial. Assume that the delta distribution be expressed in terms as a series of the Hermite function

$$\mathsf{d}_{\mathsf{r}}(x) = \sum_{n=0}^{\infty} c_n h_n\left(\frac{x}{\sqrt{2}\mathsf{r}}\right) \tag{8}$$

coefficient c_n can be found by

$$\begin{aligned} H_n(0) &= \int_{-\infty}^{\infty} \mathsf{d}_{\mathsf{r}}(x) H_n\left(\frac{x}{\sqrt{2}\mathsf{r}}\right) \mathrm{d}x = \sum_{m=0}^{\infty} c_m \int_{-\infty}^{\infty} \exp\left(-\frac{x^2}{2\mathsf{r}^2}\right) H_m\left(\frac{x}{\sqrt{2}\mathsf{r}}\right) H_n\left(\frac{x}{\sqrt{2}\mathsf{r}}\right) \mathrm{d}x \\ &= \sum_{m=0}^{\infty} c_m \mathsf{d}_{n,m} 2^m m! \sqrt{2}\mathsf{r}, \end{aligned} \tag{9}$$

where the orthogonality of the Hermite polynomials $\int_{-\infty}^{\infty} H_{n'}(x) H_m(x) \mathrm{e}^{-x^2}\, \mathrm{d}x = \mathsf{d}_{n,m} 2^m m! \sqrt{\pi}$ has been used. By means of the Hermite number $H_n(0)$,

$$H_n(0) = \begin{cases} \frac{(-1)^{n/2} n!}{(n/2)!}, & n \text{ even}, \\ 0, & n \text{ odd}, \end{cases} \tag{10}$$

one obtains

$$c_n = \begin{cases} \frac{1}{\mathsf{r}} \left(-\frac{1}{4}\right)^{n/2} \frac{1}{(2\pi)^{1/2}(n/2)!}, & n \text{ even}, \\ 0, & n \text{ odd}. \end{cases} \tag{11}$$

Therefore, the Hermite function representation of the delta distribution is

$$\mathsf{d}_{\mathsf{r}}(x) = \frac{1}{\mathsf{r}} \sum_{n=0}^{\infty} \left(-\frac{1}{4}\right)^n \frac{1}{\sqrt{2\pi} n!} h_{2n}\left(\frac{x}{\sqrt{2}\mathsf{r}}\right). \tag{12}$$

By using $(\mathrm{d}^l/\mathrm{d}x^l)h_n(x) = (-1)^l h_{n+l}(x)$, an expression for the lth order derivative of $\mathsf{d}_{\mathsf{r}}(x)$ is obtained

$$\mathsf{d}_{\mathsf{r}}^{(l)}(x) = \frac{(-1)^l}{2^{l/2}\mathsf{r}^{l+1}} \sum_{n=0}^{\infty} \left(-\frac{1}{4}\right)^n \frac{1}{\sqrt{2\pi} n!} h_{2n+l}\left(\frac{x}{\sqrt{2}\mathsf{r}}\right), \quad l = 0, 1, 2, \ldots \tag{13}$$

These kernels are continuous and admit the formal relation $f^{(l)}(x) = \int_{-\infty}^{\infty} \mathsf{d}_{\mathsf{r}}^{(l)}(x - x') f(x')\, \mathrm{d}x'$, which is undesirable for numerical computations. For practical computations, the summation in Eq. (9) has to be truncated to a finite number, say $M_{\mathrm{h}}/2$, just like in any other spectral method. Moreover, the integration needs to be discretized. It turns out that $\mathsf{d}_{\mathsf{r}}^{(l)}(x)$ works extremely well on a uniform grid. One therefore replaces the integration by a summation: $\int \to h\sum$. As a result, the Hermite local spectral kernels are given by

$$\mathsf{d}_{h,\mathsf{r}}^{(l)}(x - x_k) = \frac{(-1)^l h}{2^{l/2}\mathsf{r}^{l+1}} \sum_{n=0}^{M_{\mathrm{h}}} \left(-\frac{1}{4}\right)^n \frac{1}{\sqrt{2\pi} n!} h_{2n+l}\left(\frac{x - x_k}{\sqrt{2}\mathsf{r}}\right), \quad l = 0, 1, 2, \ldots. \tag{14}$$

Implemented in the same manner as other DSC kernels, given by Eq. (5), the Hermite local spectral kernel has been applied to the solution of the Fokker–Planck equations [75], incompressible and compressible Navier–Stokes equations [59]. Some mathematical analysis of the Hermite local spectral kernel was given in [76].

2.2. Local spectral evolution kernels

A family of local spectral evolution kernels (LSEKs) are constructed in this section for the analytical integration of evolution PDEs of the form

$$\frac{\partial}{\partial t} f(x,t) = L_1 f(x,t) = \left(A(t)\frac{\partial^2}{\partial x^2} + B(t)\frac{\partial}{\partial x} + C(t)\right) f(x,t), \tag{15}$$

where A, B and C are functions of time, while $\mathrm{Re}(A) \geqslant 0$. The formal solution of Eq. (15) can be given as

$$f(x,t) = \int \mathrm{d}x'\, K(x, x', t, t') f(x', t'), \tag{16}$$

where $K(x, x', t, t')$ is an evolution operator, defined as

$$K(x, x', t, t') = \left\langle x \middle| \exp\left(\int_{t'}^{t} L_1\, \mathrm{d}t\right) \middle| x' \right\rangle. \tag{17}$$

Here the standard Dirac notation [77] is used and $\langle f | g \rangle$ is defined as

$$\langle f | g \rangle = \int f^*(x) g(x)\, \mathrm{d}x, \tag{18}$$

where $\langle f | = f^*$ is a "bra vector" and $|g\rangle$ a "ket-vector".

The most important property of the evolution operator is stated in the following theorem.

Theorem 2. *The evolution operator K in its position representation $K(x, x', t, t')$ has a toeplitz matrix, i.e.,*

$$K(x, x', t, t') = K(x - x', t, t').$$

Proof 2. By means of the wavenumber operator $\mathbf{k} = -\mathrm{i}(\mathrm{d}/\mathrm{d}x)$, one can rewrite L_1 as

$$L_1 = -A(t)\mathbf{k}^2 + \mathrm{i}B(t)\mathbf{k} + C(t). \tag{19}$$

By using the orthonormality of the wavenumber basis $\int |k\rangle\langle k|\,\mathrm{d}k = 1$, we may write

$$K(x,x',t,t') = \int \mathrm{d}k \left\langle x \middle| \exp\left(\int_{t'}^{t} L_1\,\mathrm{d}t\right) \middle| k \right\rangle \langle k|x'\rangle. \tag{20}$$

Since the wavenumber basis $|k\rangle$ is the eigenfunction of the wavenumber operator $\mathbf{k}$, we write

$$\left\langle x \middle| \exp\left(\int_{t'}^{t} L_1\,\mathrm{d}t\right) \middle| k \right\rangle = \exp\left(-A_{t'}^{t}k^2 + \mathrm{i}B_{t'}^{t}k + C_{t'}^{t}\right)\langle x|k\rangle, \tag{21}$$

where we denote $X_{t'}^{t} = \int_{t'}^{t} X(s)\,\mathrm{d}s$ for $X = A$, B and C. Therefore, the evolution operator can be written as

$$K(x,x',t,t') = \int \mathrm{d}k\ \exp\left(-A_{t'}^{t}k^2 + \mathrm{i}B_{t'}^{t}k + C_{t'}^{t}\right)\langle x|k\rangle\langle k|x'\rangle. \tag{22}$$

Since the matrix of operator $\mathbf{k}$ in the position representation is given by

$$\langle x|\mathbf{k}|x'\rangle = -\mathrm{i}\frac{\mathrm{d}}{\mathrm{d}x}\mathsf{d}(x-x'), \tag{23}$$

we can obtain an explicit expression for the transfer matrix $\langle x|k\rangle$ via

$$k\langle x|k\rangle = \langle x|\mathbf{k}|k\rangle = \int \mathrm{d}x'\ \langle x|\mathbf{k}|x'\rangle\langle x'|k\rangle = -\mathrm{i}\int \mathrm{d}x'\ \frac{\mathrm{d}}{\mathrm{d}x}\mathsf{d}(x-x')\langle x'|k\rangle = -\mathrm{i}\frac{\mathrm{d}}{\mathrm{d}x}\langle x|k\rangle. \tag{24}$$

The solution to this differential equation with an appropriate normalization is

$$\langle x|k\rangle = \frac{1}{\sqrt{2\pi}}\mathrm{e}^{\mathrm{i}xk}. \tag{25}$$

By substituting Eq. (25) into Eq. (22), we have

$$K(x,x',t,t') = \frac{1}{2\pi}\int \mathrm{d}k\ \exp\left(-A_{t'}^{t}k^2 + \mathrm{i}(x-x'+B_{t'}^{t})k + C_{t'}^{t}\right). \tag{26}$$

For $A_{t'}^{t} \neq 0$, the above integration can be carried out by using a Gaussian integral,

$$\int \mathrm{d}x\ \exp(-ax^2+bx) = \sqrt{\frac{\pi}{a}}\exp\left(\frac{b^2}{4a}\right), \quad \mathrm{Re}(a) > 0. \tag{27}$$

For $A_{t'}^{t} = 0$, the integration in Eq. (26) can be carried out directly. Therefore, the evolution operator can be written as

$$\begin{aligned} K(x,x',t,t') &= \begin{cases} \frac{1}{\sqrt{4\pi A_{t'}^{t}}}\exp\left(-\frac{(x-x'+B_{t'}^{t})^2}{4A_{t'}^{t}} + C_{t'}^{t}\right) & (A \neq 0), \\ \mathsf{d}\left(x-x'+B_{t'}^{t}\right)\exp\left(C_{t'}^{t}\right) & (A = 0) \end{cases} \\ &= K(x-x',t,t'). \qquad \square \end{aligned} \tag{28}$$

With the aid of Theorem 2, we can consider a Hermite function representation of the evolution operator $K(x-x',\,t)$ by using $\mathsf{d}_{h,\mathsf{r}}(x)$,

$$K_{h,\mathsf{r}}(x,t,t') = \int \mathrm{d}x'\ K(x-x',t,t')\mathsf{d}_{h,\mathsf{r}}(x') \tag{29}$$

$$= \int \mathrm{d}x'\ K(x-x',t,t')\frac{h}{\mathsf{r}}\sum_{n=0}^{M_{\mathrm{h}}}\left(-\frac{1}{4}\right)^{n}\frac{1}{\sqrt{2\pi n!}}h_{2n}\left(\frac{x'}{\sqrt{2}\mathsf{r}}\right)$$

$$= \frac{h}{\mathsf{r}}\sum_{n=0}^{M_{\mathrm{h}}/2}\left(-\frac{1}{4}\right)^{n}\frac{1}{\sqrt{2\pi n!}}\mathsf{H}_{2n}(x,t,t'), \tag{30}$$

where

$$\mathsf{H}_{2n}(x,t,t') = \int \mathrm{d}x'\, K(x,x',t,t') h_{2n}\left(\frac{x'}{\sqrt{2}\mathsf{r}}\right). \tag{31}$$

To arrive at an explicit expression for the local spectral evolution kernel $K_{h,\,\mathsf{r}}(x,\,t,\,t')$, we need the following theorem.

Theorem 3. *The Hermite function $h_{2n}(x)$ is invariant under the action of the evolution operator $K(x,\,x',\,t,\,t')$.*

Proof 3. For $A = 0$, the integration in Eq. (31) can be carried out directly by using the result of Theorem 2 to give $\mathsf{H}_{2n}(x,t,t') = \mathrm{e}^{C'_{t'}} h_{2n}(\frac{x+B^t_{t'}}{\sqrt{2}\mathsf{r}})$. We therefore consider the case of $A \neq 0$. From Eq. (17), $K(x,\,x',\,t,\,t')$ can also be written as

$$K(x,x',t,t') = \mathsf{d}(x-x') \exp\left(A^t_{t'}\frac{\mathrm{d}^2}{\mathrm{d}x'^2} + B^t_{t'}\frac{\mathrm{d}}{\mathrm{d}x'} + C^t_{t'}\right), \tag{32}$$

where use is made for the orthogonality of the position basis $\langle x|x'\rangle = \mathsf{d}(x-x')$. Combining Eqs. (31) and (32), one obtains

$$\mathsf{H}_{2n}(x,t,t') = \exp\left(A^t_{t'}\frac{\mathrm{d}^2}{\mathrm{d}x^2} + B^t_{t'}\frac{\mathrm{d}}{\mathrm{d}x} + C^t_{t'}\right) h_{2n}\left(\frac{x}{\sqrt{2}\mathsf{r}}\right). \tag{33}$$

By using the generating formula of the Hermite function,

$$h_n(x) = (-1)^n \frac{\mathrm{d}^n}{\mathrm{d}x^n}\exp(-x^2), \tag{34}$$

and the fact that the nth derivative with respect to x commutes with $\exp(A^t_{t'}\frac{\partial^2}{\partial x^2} + B^t_{t'}\frac{\partial}{\partial x} + C^t_{t'})$, one can rewrite $\mathsf{H}_{2n}(x,\,t,\,t')$ as

$$\mathsf{H}_{2n}(x,t,t') = (\sqrt{2}\mathsf{r})^{2n}\frac{\mathrm{d}^{2n}}{\mathrm{d}x^{2n}} \exp\left(A^t_{t'}\frac{\mathrm{d}^2}{\mathrm{d}x^2} + B^t_{t'}\frac{\mathrm{d}}{\mathrm{d}x} + C^t_{t'}\right)\exp\left(-\frac{x^2}{2\mathsf{r}^2}\right). \tag{35}$$

By using $f(x) = \int \mathrm{d}x'\, \mathsf{d}(x-x')f(x')$, one may write

$$\mathsf{H}_{2n}(x,t,t') = (\sqrt{2}\mathsf{r})^{2n}\frac{\mathrm{d}^{2n}}{\mathrm{d}x^{2n}} \int \mathrm{d}x'\, \mathsf{d}(x-x') \exp\left(A^t_{t'}\frac{\mathrm{d}^2}{\mathrm{d}x^2} + B^t_{t'}\frac{\mathrm{d}}{\mathrm{d}x} + C^t_{t'}\right)\exp\left(-\frac{x'^2}{2\mathsf{r}^2}\right). \tag{36}$$

Combining Eqs. (32) and (36), we have

$$\mathsf{H}_{2n}(x,t,t') = (\sqrt{2}\mathsf{r})^{2n}\frac{\mathrm{d}^{2n}}{\mathrm{d}x^{2n}} \int \mathrm{d}x'\, K(x,x',t,t')\exp\left(-\frac{x'^2}{2\mathsf{r}^2}\right). \tag{37}$$

By substituting the result of Theorem 2 in Eq. (28) for $K(x,\,x',\,t,\,t')$, one obtains

$$\int \mathrm{d}x'\, K(x,x',t,t')\exp\left\{-\frac{x'^2}{2\mathsf{r}^2}\right\} = \frac{1}{\sqrt{4\pi A t}}\exp\left\{-\frac{(x+B^t_{t'})^2}{4A^t_{t'}} + C^t_{t'}\right\}\int \mathrm{d}x'\, \exp\left\{-C_1 x'^2 + C_2 x'\right\}, \tag{38}$$

where

$$C_1 = \frac{1}{2\mathsf{r}^2} + \frac{1}{4A^t_{t'}}, \quad C_2 = \frac{x+B^t_{t'}}{2A^t_{t'}}. \tag{39}$$

By using the Gaussian integral, one attains

$$\int \mathrm{d}x'\, K(x,x',t,t') \exp\left(-\frac{x'^2}{2\mathsf{r}^2}\right) = \mathrm{e}^{C_{t'}^t} \frac{\mathsf{r}}{\mathsf{r}_t} \exp\left(-\frac{(x+B_{t'}^t)^2}{2(\mathsf{r}_{t'}^t)^2}\right), \tag{40}$$

where, we denote

$$(\mathsf{r}_{t'}^t)^2 = \mathsf{r}^2 + 2A_{t'}^t.$$

Substituting Eq. (40) into Eq. (37), one obtains

$$\mathsf{H}_{2n}(x,t,t') = (\sqrt{2}\mathsf{r})^{2n} \mathrm{e}^{C_{t'}^t} \frac{\mathsf{r}}{\mathsf{r}_{t'}^t} \frac{\mathrm{d}^{2n}}{\mathrm{d}x^{2n}} \exp\left(-\frac{(x+B_{t'}^t)^2}{2(\mathsf{r}_{t'}^t)^2}\right). \tag{41}$$

By using the generating formula (34),

$$\mathsf{H}_{2n}(x,t,t') = \begin{cases} \mathrm{e}^{C_{t'}^t} \left(\frac{\mathsf{r}}{\mathsf{r}_{t'}^t}\right)^{2n+1} h_{2n}\left(\frac{x+B_{t'}^t}{\sqrt{2}\mathsf{r}_{t'}^t}\right), & A \neq 0, \\ \mathrm{e}^{C_{t'}^t} h_{2n}\left(\frac{x+B_{t'}^t}{\sqrt{2}\mathsf{r}}\right), & A = 0. \end{cases} \tag{42}$$

□

With Theorem 3 and Eq. (30), the LSEK can be explicitly given by

$$K_{h,\mathsf{r}}(x,t,t') = \frac{h}{\mathsf{r}} \mathrm{e}^{C_{t'}^t} \sum_{n=0}^{M_{\mathrm{h}}/2} \left(-\frac{1}{4}\right)^n \frac{1}{\sqrt{2\pi}n!} \left(\frac{\mathsf{r}}{\mathsf{r}_{t'}^t}\right)^{2n+1} h_{2n}\left(\frac{x+B_{t'}^t}{\sqrt{2}\mathsf{r}_{t'}^t}\right). \tag{43}$$

The case of $A = 0$ can be recovered by setting $\mathsf{r}_{t'}^t = \mathsf{r}$.

The following corollary extends some of these results to other DSC kernels.

Corollary 1. *For* $A = 0$, *the* LSEK *takes the form of*

$$K_{h,\mathsf{r}}(x,t,t') = \mathrm{e}^{C_{t'}^t} \mathsf{d}_{h,\mathsf{r}}\left(x + B_{t'}^t\right), \tag{44}$$

where $\mathsf{d}_{h,\mathsf{r}}(x)$ *can be any one of the DSC kernels given by Eqs.* (2)–(4) *and* $\mathsf{d}_{h,\mathsf{r}}^{(0)}$ *of Eq.* (14).

Proof 4. The proof follows from Eq. (29) and Theorem 2. □

In fact, an exact solution is readily available for Eq. (15).

Corollary 2. *The evolution PDE given in Eq.* (15) *admits an exact solution*

$$f(x,t) = \mathrm{e}^{C_{t'}^t} \frac{\mathsf{r}}{\mathsf{r}_t} \exp\left(-\frac{(x+B_{t'}^t)^2}{2(\mathsf{r}_{t'}^t)^2}\right), \tag{45}$$

providing that the initial value takes the form

$$f(x,0) = \exp\left(-\frac{x^2}{2\mathsf{r}^2}\right). \tag{46}$$

Proof 5. The proof follows from Eqs. (16) and (40). □

Remark 1. Many exact solutions associated with other initial values can be derived by using the present procedure.

Remark 2. A simplification of $K_{h,\,\mathsf{r}}(x,\,t,\,t')$ occurs when A, B and C are independent of time, i.e., $X(t) = X$ for $X = A$, B and C. Then, $X_{t'}^t = X(t-t') = X\Delta t$, and $K_{h,\,\mathsf{r}}(x,\,t,\,t') = K_{h,\,\mathsf{r}}(x,\,t-t') = K_{h,\,\mathsf{r}}(x,\,\Delta t)$.

Remark 3. When $A = B = C = 0$, the LSEK reduces to the local spectral interpolation kernel, $\mathsf{d}^{(0)}_{h,\mathsf{r}}(x - x_k)$, given in Eq. (14).

Remark 4. In general, Eq. (15) does not admit an exact solution for an arbitrary initial function $f(x, t')$. Then the solution $f(x, t)$ of Eq. (15) at an arbitrary space–time position (x, t) can be analytically approximated by

$$f(x,t) = \sum_{k=-M}^{M} K_{h,\mathsf{r}}(x - x_k, t, t') f(x_k, t'), \tag{47}$$

or for a grid point (x_j, t)

$$f(x_j,t) = \sum_{k=-M}^{M} K_{h,\mathsf{r}}(kh, t, t') f(x_j - kh, t'). \tag{48}$$

The LSEK is implemented in the same manner as other local spectral kernels, given by Eq. (5). Note that the CFL constraint does not apply to Eq. (48). In fact, both forward and backforward time evolutions can be resolved by using the LSEK as long as $\mathrm{Re}(\mathsf{r}^{t}_{t'}) \geqslant 0$ for a given t.

Remark 5. The LSEK can be easily generalized to an arbitrarily high dimension by the tensorial product. For example, in 2D, one has

$$f(x_i,y_j,t) = \sum_{k_x=-M_x}^{M_x} \sum_{k_y=-M_y}^{M_y} K_{h_x,\mathsf{r}_x}(k_x h_x, t, t') K_{h_y,\mathsf{r}_y}(k_y h_y, t, t') f(x_i - k_x h_x, y_j - k_y h_y, t'), \tag{49}$$

where definitions of quantities with subscripts are self-evident. The LSEK provides a convenient tool for constructing local spectral time splitting methods. Its parameter dependence is studied next.

2.3. Analyses of the LSEK

The properties of the LSEK are analyzed in this section. Dispersion analysis via the Fourier transform is a classic approach for characterizing digital filters and computational schemes. Both infinite and discrete Fourier transforms can be used. Since numerical computations are carried out on discrete grids, the discrete Fourier transform is more appropriate for the understanding of many numerical properties, such as truncation errors. The behavior of the LSEK is determined by three functions in the evolution PDEs, A, B and C, and by the DSC parameters, M_{h}, M and r. As $C(t)$ simply causes exponential decay or growth and its effect is obvious, we set $C(t) = 0$ in the Fourier analysis. We therefore discuss the discrete Fourier analysis for four different combinations of A and B: (1) $A(t) = B(t) = C(t) = 0$; (2) $B(t) = C(t) = 0$ and $A(t)$ is a real-valued function; (3) $B(t) = C(t) = 0$ and $A(t)$ is a purely imaginary function; (4) $C(t) = 0$ and $B(t) \neq 0$. In the rest of this section, the magnitude of the frequency response is defined as $|\hat{K}_{h,\mathsf{r}}(\mathsf{x})|$, where $\hat{K}_{h,\mathsf{r}}(\mathsf{x})$ denotes the discrete Fourier transform of the LSEK, $K_{h,\mathsf{r}}(x, t, t')$, given in Eq. (43).

2.3.1. $A(t) = B(t) = C(t) = 0$

As mentioned in Remark 3, when $A(t) = B(t) = C(t) = 0$, the property of the LSEK is just that of the local spectral interpolation kernel $\mathsf{d}^{(0)}_{h,\mathsf{r}}$. Unlike most global spectral methods that admit irregular mesh nodes computed according to the roots of the highest degree polynomial, local spectral methods employ a uniform grid mesh. Consequently, the scaling parameter r has to been chosen appropriately so that an optimal computational efficiency can be achieved. For a given M_{h}, an optimal r can be found according to the central frequency π/h. Specifically, for different M_{h}, one takes $\mathsf{r}/h = r$, where r varies according to M_{h}. Table 1 gives a summary of recommended r values for a wide range of M_{h} values ($1 \leqslant M_{\mathrm{h}} \leqslant 200$).

Table 1
Recommended $r = \mathsf{r}/h$ values for different M_h

M_h	r	M_h	r	M_h	r	M_h	r
1	0.70	51	2.32	101	3.27	151	3.96
2	0.80	52	2.34	102	3.28	152	3.98
3	0.90	53	2.36	103	3.30	153	3.99
4	1.00	54	2.38	104	3.32	154	4.01
5	1.05	55	2.40	105	3.33	155	4.02
6	1.10	56	2.42	106	3.34	156	4.04
7	1.15	57	2.45	107	3.35	157	4.06
8	1.18	58	2.47	108	3.37	158	4.07
9	1.22	59	2.49	109	3.38	159	4.08
10	1.27	60	2.51	110	3.40	160	4.09
11	1.30	61	2.53	111	3.42	161	4.10
12	1.34	62	2.55	112	3.44	162	4.11
13	1.37	63	2.57	113	3.45	163	4.12
14	1.40	64	2.59	114	3.46	164	4.14
15	1.43	65	2.61	115	3.47	165	4.15
16	1.47	66	2.63	116	3.48	166	4.16
17	1.50	67	2.65	117	3.49	167	4.17
18	1.54	68	2.67	118	3.51	168	4.18
19	1.57	69	2.69	119	3.53	169	4.19
20	1.60	70	2.71	120	3.55	170	4.20
21	1.62	71	2.73	121	3.56	171	4.22
22	1.64	72	2.75	122	3.58	172	4.23
23	1.66	73	2.77	123	3.59	173	4.24
24	1.68	74	2.80	124	3.60	174	4.25
25	1.70	75	2.82	125	3.61	175	4.26
26	1.72	76	2.84	126	3.63	176	4.28
27	1.75	77	2.86	127	3.64	177	4.29
28	1.78	78	2.88	128	3.66	178	4.30
29	1.80	79	2.90	129	3.67	179	4.31
30	1.82	80	2.92	130	3.69	180	4.33
31	1.84	81	2.94	131	3.70	181	4.34
32	1.87	82	2.95	132	3.71	182	4.35
33	1.89	83	2.96	133	3.72	183	4.36
34	1.91	84	2.98	134	3.74	184	4.37
35	1.94	85	3.00	135	3.75	185	4.38
36	1.96	86	3.02	136	3.77	186	4.39
37	1.98	87	3.04	137	3.78	187	4.41
38	2.01	88	3.05	138	3.79	188	4.42
39	2.05	89	3.06	139	3.80	189	4.43
40	2.08	90	3.07	140	3.81	190	4.44
41	2.10	91	3.09	141	3.83	191	4.45
42	2.11	92	3.11	142	3.85	192	4.47
43	2.13	93	3.13	143	3.86	193	4.48
44	2.15	94	3.15	144	3.87	194	4.49
45	2.18	95	3.17	145	3.89	195	4.50
46	2.20	96	3.19	146	3.90	196	4.51
47	2.23	97	3.20	147	3.91	197	4.52
48	2.26	98	3.22	148	3.93	198	4.54
49	2.28	99	3.24	149	3.94	199	4.55
50	2.30	100	3.25	150	3.95	200	4.57

In practical applications, a three percent derivation from the recommended r values will not significantly change the computational result. In the rest of this section, we set $M_{\mathrm{h}} = 88$, $h = 0.3125$ and $\mathsf{r} = 3.05h$, unless specified.

2.3.2. $A(t)$ is a real-valued function and $B(t) = C(t) = 0$

The frequency responses of the LSEK with different $A^t_{t'}$ are plotted in Fig. 1. As one can see, when $A^t_{t'}$ equals zero or is very small, the LSEK is almost an ideal low-pass filter, which suggests that the LSEK is stable and is of spectral accuracy. When $A^t_{t'}$ becomes larger, the frequency response becomes narrower. It is interesting to note that this does not cause the loss of accuracy of the LSEK method for integrating the diffusion equation. Because when $A(t)$ is a real-valued function, the dynamics of the diffusion process assures that the high frequency components of the solution vanish after a certain time period. The decay rates of the high frequency components of both the LESK and the solution of the diffusion equation (62) are studied. Their frequency responses are compared in Fig. 2 by setting $A(t) = D$, where D is the diffusion coefficient. It can be seen that the frequency response of the solution is always within the boundary of that of the LSEK. As time or $A^t_{t'}$ increases, the frequency response of the solution becomes narrower and narrower

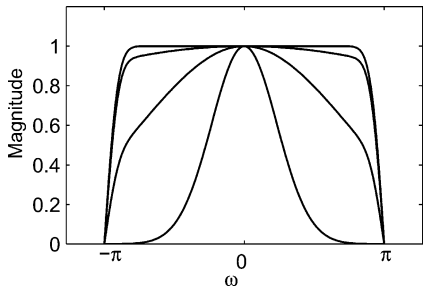

Fig. 1. The frequency responses of the LSEK when $B(t) = C(t) = 0$ ($M = 64$, $M_{\mathrm{h}} = 88$). The solid lines from outside to inner are for $A^t_{t'} = 0,\ 0.001\mathsf{r}^2,\ 0.01\mathsf{r}^2,\ 0.1\mathsf{r}^2$.

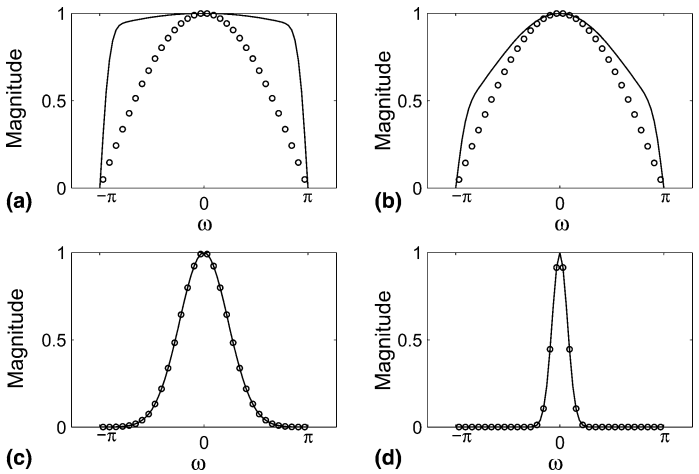

Fig. 2. The comparison of the frequency responses of the LSEK, 'solid line', and the frequency responses of the solution of the Wiener process, 'circle' ($M = 64$, $M_{\mathrm{h}} = 88$, $B(t) = C(t) = 0$, $A^t_{t'} = D(t - t_0)$). (a) $A^t_{t'} = 0.001\mathsf{r}^2$; (b) $A^t_{t'} = 0.01\mathsf{r}^2$; (c) $A^t_{t'} = 0.1\mathsf{r}^2$ and (d) $A^t_{t'} = \mathsf{r}^2$.

because only low frequency components could survive for a long time diffusion. In addition, the frequency responses of the LSEK and the solution overlap when time or $A^t_{t'}$ is sufficiently larger.

The frequency responses of the LSEK with different M_h are plotted in Fig. 3, when $A(t) = 0$. As one can see, an almost ideal low-pass filter is obtained at $M_h = 88$. When M_h is smaller than 88, the smaller M_h is, the narrower the bandwidth of the frequency response is. This is because a larger M_h means the use of higher degree Hermite polynomials that provide a better approximation to high frequency components. However, for a given r, when M_h is larger than 88, the larger M_h is, the narrower the bandwidth is obtained. This is an interesting behavior of the Hermite local spectral method. Obviously, the superposition of higher degree Hermite polynomials cancels the high frequency components of the LSEK. This happens because in our local spectral method, a uniform mesh is always used, instead of the non-uniform Gauss–Hermite nodes computed according to the highest degree of the polynomial. Therefore, for a given choice of r, an optimized M_h is quite important in the present local spectral method. Fortunately, there exists essentially a linear relation between r, and its optimized M_h as shown in Table 1. The frequency responses of the LSEK with different M are plotted in Fig. 4. It can be seen that $M = 32$ is good enough to give an accurate approximation.

2.3.3. $A(t)$ is a purely imaginary function and $B(t) = C(t) = 0$

The frequency responses of the LSEK with different $A^t_{t'}$ are plotted in Fig. 5. The time evolution of the frequency responses in this case is quite different from the ones in Fig. 1. When parameters M and M_h are fixed, the low frequency part of the responses is flat when $A^t_{t'} = 0, 0.1\mathsf{i}\mathsf{r}^2, 0.5\mathsf{i}\mathsf{r}^2$. The increase of $A^t_{t'}$ only

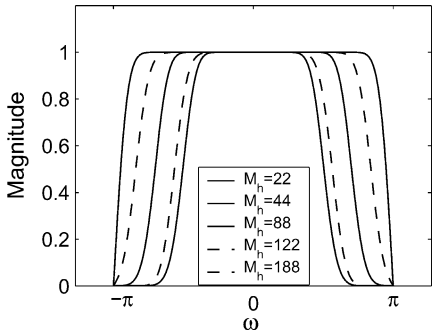

Fig. 3. The frequency responses of the LSEK with different M_h ($A(t) = B(t) = C(t) = 0$, $M = 64$). 'Solid lines' represent $M_h = 22, 44, 88$ from innermost to outside; 'dash lines' represent $M_h = 122,188$ from outside to inner.

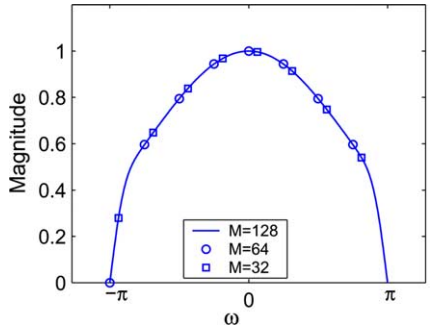

Fig. 4. The frequency responses of the LSEK with different M. $A^t_{t'} = 0.01\mathsf{r}^2$, $B(t) = C(t) = 0$, $M_h = 88$.

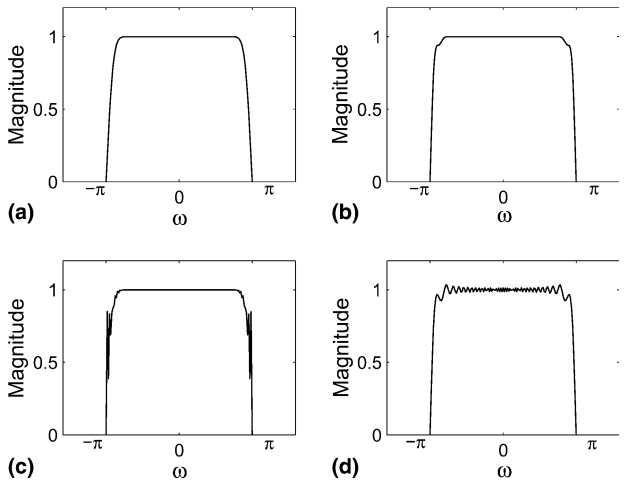

Fig. 5. The frequency responses of the LSEK with different $A^t_{t'}(B(t) = C(t) = 0,\ M = 64,\ M_h = 88)$. (a) $A^t_{t'} = 0$; (b) $A^t_{t'} = 0.1i\mathsf{r}^2$; (c) $A^t_{t'} = 0.5i\mathsf{r}^2$ and (d) $A^t_{t'} = i\mathsf{r}^2$.

generates some oscillations over small intervals near $\pm\pi$. In other words, the LS method is capable of providing spectral accuracy to most problems that do not have a very high frequency component. While when $A^t_{t'} = i\mathsf{r}^2$, the low frequency part becomes oscillatory, which is due to the truncation. Essentially, a large $A^t_{t'}$ gives rise to a large $\mathsf{r}^t_{t'}$, and thus a larger spatial extension for a given Hermite polynomial. In such a case, the fixed spatial support $2M + 1$ is no longer large enough and the truncation error becomes evident. The truncation error can be efficiently reduced by simply increasing M, the half length of the spatial support of the LSEK. Fig. 6 shows the dependence of the frequency responses on M. It can be seen that the low frequency parts of the responses are flat and are unity when $M = 128$ and $M = 256$. In other words, by increasing M to a sufficiently large value, the LS method could always approach spectral accuracy in one time step even when $A(t)$ or time t is very large. On the other hand, $M = 128$ and $M = 256$ does not

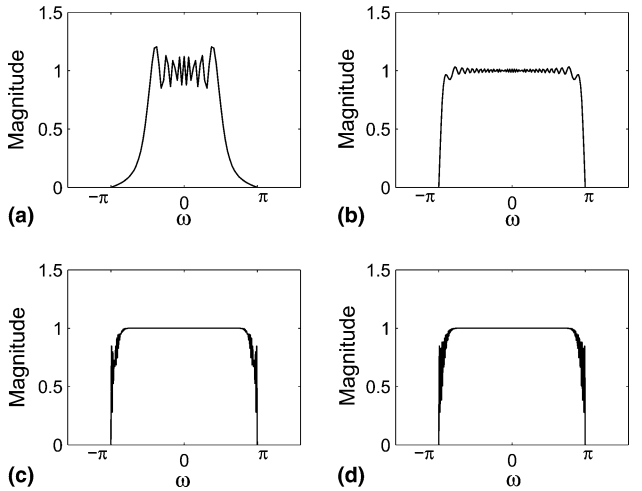

Fig. 6. The frequency responses of the LSEK with different $M(A^t_{t'} = i\mathsf{r}^2,\ B(t) = C(t) = 0,\ M_h = 88)$. (a) $M = 32$; (b) $M = 64$; (c) $M = 128$ and (d) $M = 256$.

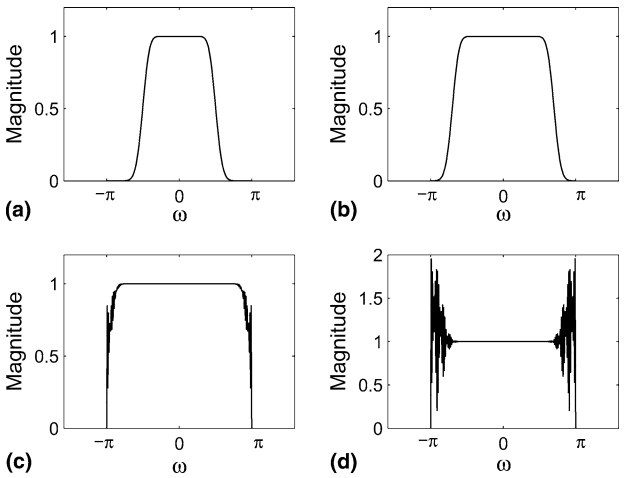

Fig. 7. The frequency responses of the LSEK with different $M_h(A^t_{t'} = r^2 i,\ B(t) = C(t) = 0,\ M = 128)$. (a) $M_h = 22$; (b) $M_h = 44$; (c) $M_h = 88$ and (d) $M_h = 122$.

make much difference in high frequency edges near $\pm\pi$. The oscillation in these regions can be explained by the mismatch of the parameters M and M_h. This fact can also be seen in Figs. 7 and 8. Fortunately, this does not cause much problems in real applications because the grid spacing h can always be slightly reduced if the frequency distribution of a physical problem is non-zero at the high frequency edges.

The frequency responses of the LSEK with different M_h, when $M = 128$ and $M = 64$ are plotted in Figs. 7 and 8, respectively. It is seen that in Fig. 7, for a given M, a smaller M_h gives a better approximation to a narrower range of the frequency distribution. When M_h is sufficiently large as shown in Fig. 7(c), a good approximation can be achieved by the LS method. However, if M_h is too large, oscillation occurs. Such oscillation is also due to the truncation. Essentially, for a given r, higher degree Hermite polynomials spatially extend to a larger effective domain and require a larger interval of compact support than do the low

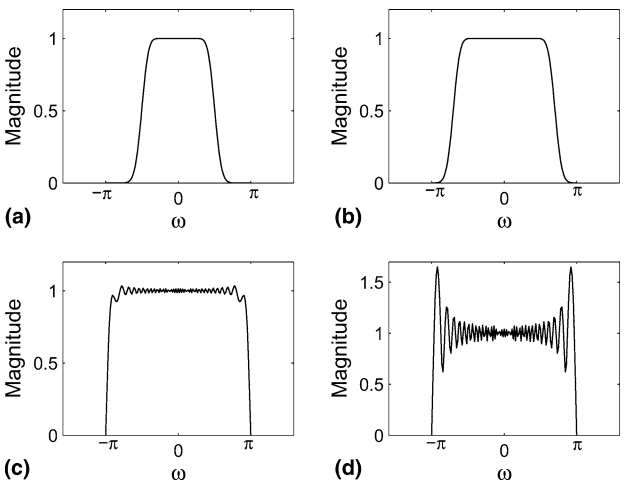

Fig. 8. The frequency responses of the LSEK with different $M_h(A^t_{t'} = r^2 i,\ B(t) = C(t) = 0,\ M = 64)$. (a) $M_h = 22$; (b) $M_h = 44$; (c) $M_h = 88$ and (d) $M_h = 122$.

degree Hermite polynomials. This problem can be alleviated in two ways. One way is to use a smaller r so that the spatial extension of high degree Hermite polynomials is reduced. The other way is to reduce truncation error directly by choosing a larger M.

The oscillation in Fig. 8 is more severe because the support $2M + 1$ is relatively too small. Therefore, if a smaller M is used, a choice of $M_h = 44$ can even give a better approximation than does $M_h = 88$ because at least the low frequency part is less corrupted by the truncation.

2.3.4. $C(t) = 0$ and $B(t) \neq 0$

The frequency responses of the LSEK with different $B^t_{t'}$, when $A(t) = C(t) = 0$ are plotted in Fig. 9. It is seen that the magnitude of the frequency response does not change as $B^t_{t'}$ changes. This is because the change of $B^t_{t'}$ can only produce a spatial translation which leads to a phase shift in the frequency responses, i.e., $e^{i\times B^t_{t'}}$. Therefore, an arbitrarily large $B(t)$ does not have any impact on the computational accuracy of the LS method. The same conclusion can be drawn for the case of $A(t) \neq 0$ and $B(t) \neq 0$, which is investigated in Fig. 10.

2.4. High-order time-splitting methods

Given a differential equation, which can be written in the form

$$f_t = L_1 f + L_2 f, \tag{50}$$

where we denote f_t for both derivative and partial derivative of f with respect to time t. Operators L_1 and L_2 can be general linear or nonlinear operators and there is no requirement that L_1 and L_2 commute.

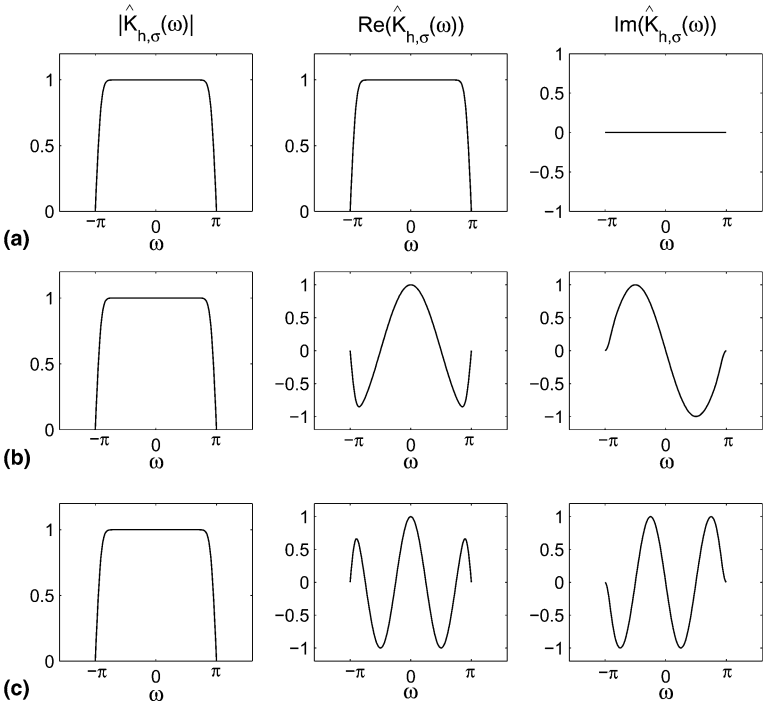

Fig. 9. The frequency responses of the LSEK with different $B^t_{t'}(M = 64,\ M_h = 88,\ A(t) = C(t) = 0)$. (a) $B^t_{t'} = 0$; (b) $B^t_{t'} = h$ and (c) $B^t_{t'} = 2h$.

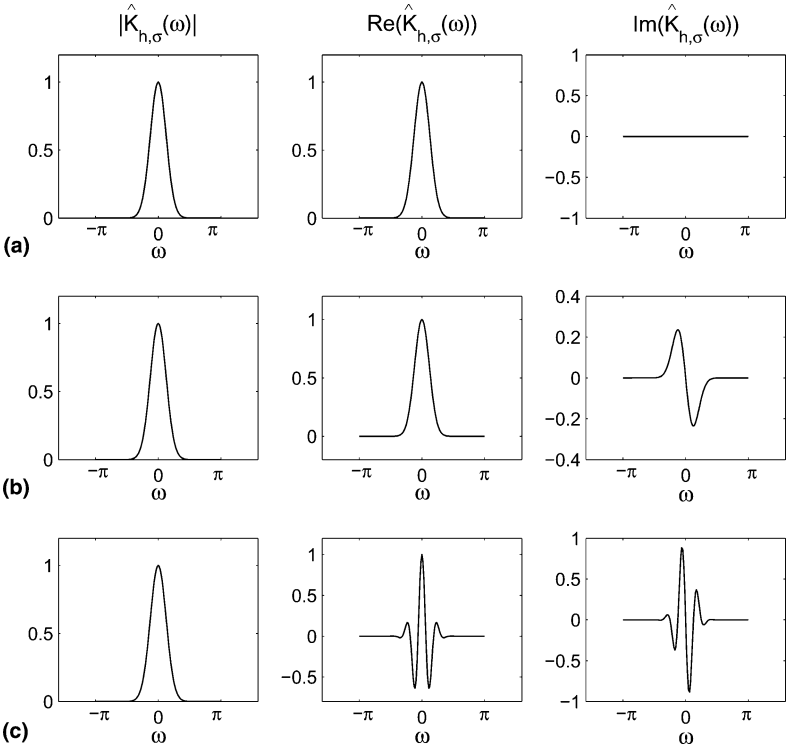

Fig. 10. The frequency responses of the LSEK with different $B^t_{t'}(M = 64,\ M_h = 88,\ A^t_{t'} = h,\ C(t) = 0)$. (a) $B^t_{t'} = 0$; (b) $B^t_{t'} = h$ and (c) $B^t_{t'} = 2h$.

The equation can be solved by a first-order time-splitting method from time t to time $t + \Delta t$ in two steps. One first solves

$$f_t = 2L_1 f \tag{51}$$

from t to $t + \frac{1}{2}\Delta t$, followed by solving

$$f_t = 2L_2 f \tag{52}$$

from $t + \frac{1}{2}\Delta t$ to $t + \Delta t$.

The two time increments are each of length $(1/2)\Delta t$, which are denoted by $\{1/2, 1/2\}$. The second-order method, which is known as "Strang splitting" [12], can be obtained by three steps. One first solves

$$f_t = 2L_1 f \tag{53}$$

from t to $t + \frac{1}{4}\Delta t$, followed by solving

$$f_t = 2L_2 f \tag{54}$$

from $t + \frac{1}{4}\Delta t$ to $t + \frac{3}{4}\Delta t$, then followed by solving

$$f_t = 2L_1 f \tag{55}$$

from $t + \frac{3}{4}\Delta t$ to $t + \Delta t$ again. The three time increments are $\{1/4, 1/2, 1/4\}$.

A systematic way to obtain high-order time-splitting methods was given by Yoshida [16]. The coefficients of methods of orders 1, 2, 4, 6 and 8 are listed in Table 2 [29]. Only the first half coefficients of the methods

Table 2
The first half coefficients of the time-splitting method

Method	Time increment sequence	
TS1	0.50000 00000 00000 00000	
TS2	0.25000 00000 00000 00000	0.50000 00000 00000 00000
TS4	0.33780 17979 89914 40851	0.67560 35959 79828 81702
	−0.08780 17979 89914 40851	−0.85120 71919 59657 63405
TS6	0.19612 84026 19389 31595	0.39225 68052 38778 63191
	0.25502 17059 59228 84938	0.11778 66066 79679 06684
	−0.23552 66927 04878 21832	−0.58883 99920 89435 50347
	0.03437 65841 26260 05298	0.65759 31603 41955 60944
TS8	0.22871 10615 57447 89169	0.45742 21231 14895 78337
	0.29213 43956 99000 73022	0.12684 66682 83105 67707
	−0.29778 97250 73598 45089	−0.72242 61184 30302 57885
	−0.40077 32180 57163 83322	−0.07912 03176 84025 08760
	0.44497 46255 63618 95284	0.96906 95688 11262 99329
	−0.00561 77738 38196 20526	−0.98030 51164 87655 40380
	−0.46445 25958 95878 59173	0.05139 99246 95898 22035
	0.45281 32300 44769 50634	0.85422 65353 93640 79233

"TS" represents time-splitting method; "1,2,4,6,8" represents the first-, second-, fourth-, sixth- and eighth-order TS method.

is given because all the coefficients are of central symmetry. For example, the fourth-order method has four different coefficients, namely C_1, C_2, C_3, C_4, then one needs solve two equations alternatively in seven steps while using the time increments $\{C_1, C_2, C_3, C_4, C_3, C_2, C_1\}$. Respectively, the sixth-order method needs 15 steps and the eighth-order method needs 31 steps to advance the equation from time t to time $t + \Delta t$.

The above algorithm of the time-splitting (TS) method is commonly used to integrate many types of partial differential equations because it is explicit and easy to program, requires less memory and is of high accuracy. In additional, if the split steps which described by Eqs. (51) and (52) can be solved exactly, unconditional stability can always be achieved by this method. For example, in simulating Nonlinear Schrödinger systems (NLS), the split steps usually can be solved analytically by using the Fourier spectral method. Therefore, in this area, the TS method is predominantly used, rather than the Crank–Nicolson method or the Runge–Kutta method, as the TS method is often more efficient.

2.5. The local spectral time-splitting method

Assume that a differential equation be written in the form

$$f_t = L_1 f + L_2(f) f = \left(A(t) \frac{\partial^2}{\partial x^2} + B(t) \frac{\partial}{\partial x} + C(t) \right) f + L_2(f) f. \tag{56}$$

where L_2 is a general operator, which can be a function of f.

This equation can be solved from time t_0 to t by the LSTS method. First of all, the PDE is splitted into two equations:

$$f_t = \left(2A(t) \frac{\partial^2}{\partial x^2} + 2B(t) \frac{\partial}{\partial x} + 2C(t) \right) f \tag{57}$$

and

$$f_t = 2L_2(f) f. \tag{58}$$

If Eq. (58) can also be solved analytically, the time splitting scheme is unconditionally stable. Alternatively solving Eqs. (57) and (58) in several split steps, one obtains a high-order LSTS method.

Let us write the solution of Eq. (58) with initial condition $f(x_0, t_0)$ as

$$f(x,t) = G(x, t - t_0, f(x_0, t_0)). \tag{59}$$

A pseudo-code of a second LSTS method for solving Eq. (56) from time t_0 to T is the follows:

- *Stage* 1. Generate the LSEK $K_{h,\,\mathrm{r}}(x, t, t')$ by Eq. (43).
- *Stage* 2. Generate the initial condition: $f_i = f(x_i, t_0)$.
- *Stage* 3. The recursion
  - **DO** $k = 1$, $(T - t_0)/\Delta t$
    - Solve Eq. (58) in $\frac{1}{4}\Delta t : f_i = 2G(i, \frac{1}{4}\Delta t, f_i)$
    - Solve Eq. (57) in $\frac{1}{2}\Delta t : f_i = \sum_{j=-M}^{M} K_{h,\mathrm{r}}(\Delta x, t + \frac{1}{2}\Delta t, t) f_j$ with $\Delta x = (i - j) * h$ and $t = (k - 1) * \Delta t + \frac{1}{4}\Delta t$.
    - Solve Eq. (58) in $\frac{1}{4}\Delta t : f_i = 2G(i, \frac{1}{4}\Delta t, f_i)$
  - **END DO**

Note that, in long time integrations, we just need to compute the set of LSEK weights once. In the case that Eq. (58) cannot be integrated analytically, the numerical solution can be used in split steps. In such a case, the stability constraint is still weaker than that of explicit schemes. In general, for a second-order PDE, the time splitting scheme just requires $\Delta t = \mathrm{O}(h)$, while explicit methods, such as the fourth-order Runge–Kutta method, require $\Delta t = \mathrm{O}(h^2)$ [67].

3. Validation

In this section, we consider several examples that admit exact solutions to demonstrate the usefulness, test the accuracy and explore the limitation of the proposed LSTS method. The spectral accuracy of the LSEK is tested by the Wiener process. The Black–Scholes equation is employed to examine the LSEK with non-zero convection and production coefficients. The heat equation is employed to validate the proposed method for two-dimensional (2D) computations. A free propagating plane wave governed by the Schrödinger equation is employed to investigate the parameter dependence of the LSEK. The proposed LSTS method is further validated for its stability by the Zakharov system. Finally, the performance of high-order LSTS methods is illustrated by a linear harmonic oscillator. Accuracy, stability and efficiency of the proposed method are extensively compared with those of the FPTS over different boundary conditions.

3.1. A linear hyperbolic equation

In order to validate the LSEK when $A = 0$, we consider the following linear hyperbolic equation:

$$\begin{aligned} &u_t + g(t)u_x = 0, \quad -1 < x < 1, \\ &u(x,0) = u_0(x), \quad \text{periodic}. \end{aligned} \tag{60}$$

This problem is valuable since it is analytically solvable. The exact solution for given $u(x, 0)$ can easily be derived from Eqs. (16) and (28), and is a family of traveling waves given by $u(x, t) = u_0(x, t)$ for $t \geqslant 0$. The solution $u(x, t)$ is constant along the characteristics given by a ray $x - \int g(t)\,\mathrm{d}t = x_0$. We choose $g(t) = t^2$ so

that the solution shifts sufficiently fast for large t. The initial value in the present computation is chosen as [30]

$$u_0(x) = \sin^4(\pi x). \tag{61}$$

The problem is numerically solved on interval $[-1, 1]$ by using four different methods: the LSEK realized with both the Shannon kernel and the Hermite kernel, Fourier pseudospectral (FP) method, and the FP with fourth-order Runge–Kutta (FP-RK4). The first three methods integrate the PDE in a single time step and are free of stability constraint. The errors of the LS method with the Shannon kernel and the Hermite kernel at time $t = 1, 5, 10$ are listed in Table 3, and compared with those of the other two approaches. Periodic boundary condition is used and the mesh size is set to $h = 0.0625$ in all four methods. As one can see from Table 3, the Shannon kernel and Hermite kernel yield the machine accuracy at any time and the step size can be arbitrarily large. On the contrary, the numerical solution of the FP-RK4 method blows up at time $t = 6$ even with a very small time step, $\Delta t = 0.001$.

3.2. The Wiener process

The Wiener process describes a non-stationary Markov process. The governing Fokker–Planck equation of the Wiener process can be written as

$$\frac{\partial f(x,t)}{\partial t} = D\frac{\partial^2 f(x,t)}{\partial x^2}, \tag{62}$$

where D is the diffusion coefficient. When the initial condition is the δ-function distribution at x_0, the analytical solution of Eq. (62) is

$$f(x,t) = \sqrt{\frac{1}{4D\pi(t-t_0)}}\exp\left(-\frac{(x-x_0)^2}{4D(t-t_0)}\right). \tag{63}$$

This system has been used as a standard example for testing numerical methods [75,78].

The Wiener process can be solved analytically by both the FP method and the LSEK. Therefore, numerical results are obtained in one time step by both methods. In other words, once the initial condition is given, the solution of the system at any time can be obtained without intermediate time stepping.

Table 3
Comparison of errors of four numerical methods for the hyperbolic equation

Method	t	Δt	L_∞	L_2
Shannon	1.0	1.0	8.88E − 16	4.36E − 16
	5.0	5.0	9.21E − 15	7.48E − 15
	10.0	10.0	7.47E − 14	6.69E − 14
Hermite	1.0	1.0	9.99E − 16	4.36E − 16
	5.0	5.0	8.55E − 15	6.22E − 15
	10.0	10.0	1.54E − 14	1.26E − 14
FP	1.0	1.0	9.03E − 16	7.67E − 16
	5.0	5.0	5.00E − 15	4.18E − 15
	10.0	10.0	3.71E − 14	3.17E − 14
FP-RK4	1.0	0.001	1.64E − 14	1.47E − 14
	2.5	0.001	7.63E − 7	7.13E − 7
	4.5	0.001	4.90E − 4	4.58E − 4
	6.0	0.001	–	–

Consequently, the computation is extremely fast. In addition, since there is no error caused by the time integration, the performance of the local spectral method and the FP method can be fairly compared. The LSEK adopts a Dirichlet boundary condition with an interval of $[-10, 10]$ and a mesh size $h = 0.4$. The LSEK parameters are chosen as $M = 33$, $M_h = 88$ and $r = 3.05$. Considering that the periodical boundary condition is needed for the FP method, its computational interval is taken as large as $[-12.8, 12.8]$ with the mesh size $h = 0.4$. The initial d function is localized at $x = 0$. Fig. 11 shows the time evolution of the solution. As shown in Fig. 11, the exact solutions and numerical solutions by the LSEK are graphically indistinguishable. Therefore, we further compare the L_2 and L_∞ errors for both the LSEK and the FP method. The results are listed in Table 4.

It is noted that at early time, $t = 0.6$ and $t = 0.7$, the accuracy of the Fourier pseudospectral method is slightly higher than that of the LSEK because the solution peak is very sharp. From time $t = 0.8$ to $t = 1.0$, the accuracies of two methods are almost the same, which means that the LSEK is of spectral order of accuracy for relatively smooth solutions. From time $t = 1.2$ to $t = 2.0$, the LSEK achieves even higher accuracy than the FP method does because the error induced by the periodic boundary condition in the FP method plays an important role at that time. The boundary effect is very dramatic at $t = 3.0$. Thus the LS method is more flexible in this regard (see Table 4).

3.3. The Black–Scholes equation

Black and Scholes [79] published a paper entitled "The pricing of options and corporate liabilities" in 1973. Since then the growth of the field of derivative securities has been phenomenal. The Black–Scholes'

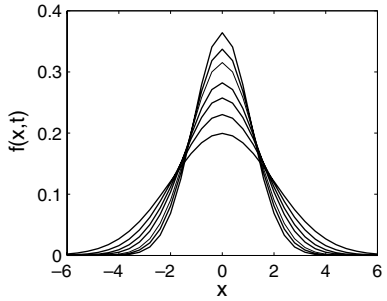

Fig. 11. The exact (dashed lines) and numerical solutions (solid lines) of the Wiener process in Section 3.2. The centerlines in the descending order are at $t = 0.6$; 0.7; 0.8; 1.0; 1.2; 1.5; 2.0.

Table 4
Errors in the numerical solution of the Wiener process

Time	LS		FP	
	L_∞	L_2	L_∞	L_2
$t = 0.6$	1.254E − 13	1.777E − 13	1.388E − 16	2.642E − 16
$t = 0.7$	4.219E − 15	6.434E − 15	1.388E − 16	2.683E − 16
$t = 0.8$	2.220E − 16	3.226E − 16	1.665E − 16	2.614E − 16
$t = 1.0$	1.665E − 16	1.812E − 16	1.735E − 16	2.768E − 16
$t = 1.2$	8.327E − 17	1.052E − 16	4.186E − 16	3.653E − 16
$t = 1.5$	9.714E − 17	1.367E − 16	3.186E − 13	2.078E − 13
$t = 2.0$	1.942E − 16	2.517E − 16	2.544E − 10	1.733E − 10
$t = 3.0$	4.362E − 13	3.995E − 13	1.915E − 7	1.445E − 7

general equilibrium formulation of the option pricing theory is attractive since the final valuation formulas deduced from their model is a function of a few observable variables (except one, which is the volatility parameter). The accuracy of the model can be ascertained by direct empirical tests with market data. The well-known Black–Scholes equation is given as [80]

$$\frac{\partial c}{\partial t} = \frac{\mathbb{m}^2}{2} S^2 \frac{\partial^2 c}{\partial S^2} + \mathbb{l} S \frac{\partial c}{\partial S} - \mathbb{l} c, \tag{64}$$

where S is the asset price which undergoes geometric Brownian motion, $c(S, t)$ is the call price, $\mathbb{m}$ is the volatility and $\mathbb{l}$ is the constant riskless interest rate. By a transformation

$$x = \ln S, \tag{65}$$

the Black–Scholes equation is cast into the following constant-coefficient parabolic equation

$$\frac{\partial c}{\partial t} = \frac{\mathbb{m}^2}{2} \frac{\partial^2 c}{\partial x^2} + \left(\mathbb{l} - \frac{\mathbb{m}^2}{2} \right) \frac{\partial c}{\partial x} - \mathbb{l} c, \quad -\infty < x < \infty, \quad t > 0. \tag{66}$$

The solution of the above equation is known to be

$$c(x,t) = \frac{1}{\mathbb{m}\sqrt{2\pi t}} \exp\left(-\frac{\left[x + \left(\mathbb{l} - \frac{\mathbb{m}^2}{2} \right) t \right]^2}{2\mathbb{m}^2 t} - \mathbb{l} t \right). \tag{67}$$

The numerical simulation of the Black–Scholes equation and its generalized versions is an important issue in financial analysis and the computational finance community [81–83] because both computational accuracy and efficiency are very important to option modeling and risk estimation. Obviously, the Black–Scholes equation is an excellent test for the proposed LSEK because it involves non-zero coefficients of diffusion, convection and production. The present method can provide both high accuracy and high efficiency for this problem because it can be solved by the LSEK in a single time step. For simplicity, we choose $(1/2)\mathbb{m}^2 = 0.5$ and $\mathbb{l} = 0.7$ in our calculations. A sufficiently large computational domain $[-10, 10]$ is used. The initial distribution is set to be the exact solution at time $t = 0.5$. Both L_2 and L_∞ error measures are used to evaluate the quality of the present method when the mesh size h is chosen as $h = 0.5$ and $h = 0.25$. As one can see, the machine accuracy is achieved, when $h = 0.25$, see Table 5. When the spatial mesh size doubles, the accuracy at time $t = 1.0$ and $t = 2.0$ is lower because the peak of the solution is quite sharp at that time such that a finer mesh strategy is needed to obtain the best approximation. As the time evolves, the solution becomes smoother such that the machine accuracy is achieved again when $h = 0.5$.

Table 5
Errors in the LS solution of the Black–Scholes equation

Time	$h = 0.5$		$h = 0.25$	
	L_2	L_∞	L_2	L_∞
1.0	4.30E − 9	2.42E − 9	5.71E − 17	5.55E − 17
2.0	2.34E − 14	2.02E − 14	5.33E − 17	5.55E − 17
3.0	3.60E − 16	2.63E − 16	1.77E − 17	2.08E − 17
4.0	3.16E − 17	2.26E − 17	3.47E − 18	4.86E − 18
5.0	5.99E − 18	5.20E − 18	4.34E − 18	5.19E − 18

3.4. 2D heat equation

The 2D heat equation is another benchmark problem because it admits the exact solution [69]. The equation can be written as

$$\frac{\partial u(x,y,t)}{\partial t} = d^2\left(\frac{\partial^2 u(x,y,t)}{\partial x^2} + \frac{\partial^2 u(x,y,t)}{\partial y^2}\right), \tag{68}$$

with an exact solution of the form

$$u(x,y,t) = \frac{1}{4d^2\pi t}\exp\left\{-\frac{(x-x_0)^2+(y-y_0)^2}{4d^2 t}\right\}. \tag{69}$$

The detailed LS method used for the 2D problem can be written as

$$u(x,y,t+\Delta t) = \sum_{j=-M}^{M}\sum_{k=-M}^{M} K_{h_x,\mathrm{r}}(x-x_j,\Delta t)K_{h_y,\mathrm{r}}(y-y_k,\Delta t)u(x_j,y_k,t). \tag{70}$$

In our computation, the heat equation is solved in a square domain $[0, 10]\times[0, 10]$. An equal spatial discretization along x- and y-directions is employed, i.e., $h = h_x = h_y = 0.3125$. The parameter d is taken as 0.7 in Eq. (68). The LSEK parameters are the same as those given in the 1D case. The point (x_0, y_0) is the center of the 2D square domain. The initial value is taken as the exact solution of the system, when $t = 0.1$. The boundary condition for the LSEK is set to be zero outside the computational domain. The computational errors with respect to the exact solution for both the LS method and the Fourier pseudospectral method are listed in Table 6. When time $t = 0.5$, the solution is sharp so that the Fourier method is slightly more accurate than the LSEK. However, the accuracy of the LSEK becomes much higher than that of the spectral method from time $t = 1.5$ to $t = 4.0$ because the periodic boundary condition used by the spectral method is not suitable anymore when time $t > 1.5$. The LSEK solutions of the heat equation at time $t = 0.5$ and $t = 2.0$ are shown in Fig. 12.

3.5. Plane wave propagation

To demonstrate the reliability of the LS method on highly oscillatory problems and to investigate the dependence of the LS parameter M, M_{h} and r on time increment and oscillation frequency, we consider the plane wave propagation process, which is governed by the Schrödinger equation

$$\mathrm{i}\frac{\partial u(x,t)}{\partial t} = \frac{\partial^2 u(x,t)}{\partial x^2}, \tag{71}$$

Table 6
Error analysis for 2D heat equation in Section 3.4

Time	LS		FP	
	L_∞	L_2	L_∞	L_2
$t = 0.5$	3.468E − 7	5.054E − 7	1.704E − 7	1.927E − 7
$t = 1.0$	3.260E − 8	6.284E − 8	4.689E − 7	9.119E − 7
$t = 1.5$	1.213E − 8	3.080E − 8	2.195E − 5	5.083E − 5
$t = 2.0$	6.771E − 9	2.117E − 8	1.380E − 4	3.722E − 4
$t = 2.5$	4.530E − 9	1.663E − 8	3.952E − 4	1.217E − 3
$t = 3.0$	3.348E − 9	1.398E − 8	7.109E − 4	2.663E − 4
$t = 4.0$	2.161E − 9	1.098E − 8	1.674E − 3	7.018E − 3

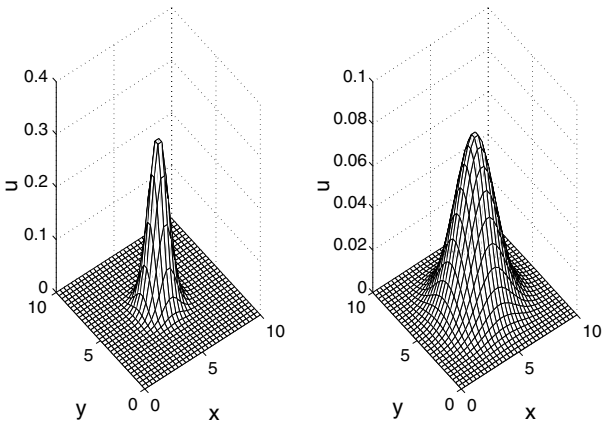

Fig. 12. LS solutions of the heat equation at time $t = 0.5$ (left chart) and $t = 2.0$ (right chart).

$$u(x,t) = u(x+L,t). \tag{72}$$

This system admits the traveling plane wave solution of the form

$$u(x,t) = A\exp(\mathrm{i}(kx - \mathsf{x}t)). \tag{73}$$

Substituting Eq. (73) into Eqs. (71) and (72), one resolves that $\mathsf{x} = -k^2$ and the wavelength $\mathsf{k} = (2\pi/k)$.

In our computation, we employ the periodic boundary condition and compute this problem in a large spatial interval $L = [0, 80]$ in one time step. A total of 512 grid points are used for this interval, i.e., $N = 512$. The initial condition is taken as the solution of the system at $t = 0$. We define PPW $= N * \mathsf{k}/L$, which represents the average number of points per wavelength. As the wavenumber k varies, PPW changes from 2.06 to 512.

Fig. 13 indicates the change of the error with respect to PPW. It is noted that when there are more than four grid points per wave, the error is less than 10^{-14} if a suitable M_{h} is chosen. Moreover, as PPW increases from 2 to 4, the error decreases *exponentially*. Stated differently, for a given wavenumber, the error of the present local spectral method decreases *exponentially* as the number of grid points increases. This is a common feature for all spectral methods [46].

Fig. 14 gives a phase diagram for the dependence of the parameter M_{h} on PPW. The parameter M_{h} represents the highest degree of Hermite polynomial used in the LS method. In order to figure out the trend of the parameter dependence of the LS method, we choose error tolerance tol $= 10^{-12}$. As it can be seen, M_{h} keeps increasing as PPW decreases because small PPW represents high oscillation which needs high degree Hermite polynomials to attain high accuracy. Fig. 15 indicates the dependence of the parameter r on PPW. The error tolerance $tol = 10^{-12}$ is also used. It is seen that the parameter r keeps increasing as PPW decreases. In another words, the higher oscillatory the solution is, the larger r is needed to achieve high accuracy. The dependence of the parameter M on PPW for given M_{h} and r is also investigated. The results show that for PPW > 4, the high accuracy can always be achieved when M equals 33. It is pointed out that there is a mismatch between parameters M_{h} and r in the above two tests. In fact, if these parameters are matched as shown in Table 1, the accuracy level of 10^{-12} can be reached with $M_{\mathrm{h}} = 10$ when PPW ~ 4.

In order to investigate the dependence of the LS parameters on the time increment Δt in the plane-wave case, we choose k such that there is only one wave in our computational domain, i.e., $\mathsf{k} = L$, PPW $= 512$. Fig. 16 indicates the dependence of the parameter M on the time increment Δt. It is noted that the

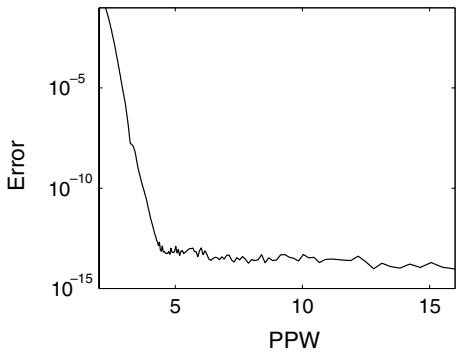

Fig. 13. The changes of the errors with respect to PPW when the parameter M_h is optimized in Section 3.5; $\Delta t = 0.01$, $M = 88$ and $r = 3.05$.

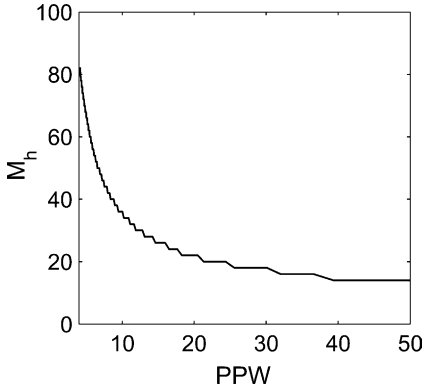

Fig. 14. A phase diagram for M_h and PPW. The errors are 1×10^{-12} on the curve, smaller than 1×10^{-12} above the curve and larger than 1×10^{-12} below the curve. Other parameters are fixed as $\Delta t = 0.01$, $M = 88$ and $r = 3.05$.

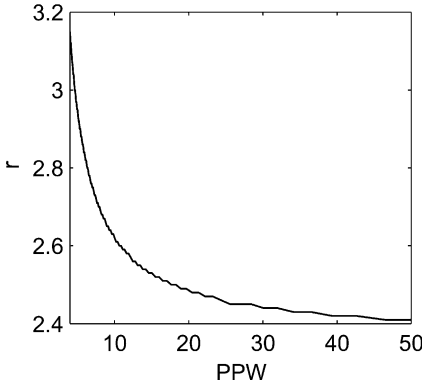

Fig. 15. A phase diagram for r and PPW. The errors are 1×10^{-12} on the curve, smaller than 1×10^{-12} above the curve and larger than 1×10^{-12} below the curve. Other parameters are fixed as $\Delta t = 0.01$, $M = 33$, $M_h = 88$.

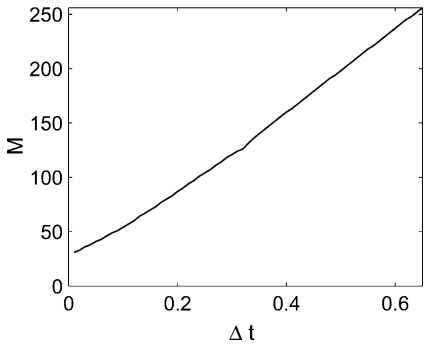

Fig. 16. The dependence of the parameter M on Δt when the error tolerance is chosen as 1×10^{-12}; PPW = 4.65, $r = 3.05$, $M_h = 88$.

parameter M linearly depends on Δt. The larger the Δt is, the larger parameter M is needed. The reason is obvious by comparing the present numerical result with the dispersion analysis in Fig. 6. A sufficiently large M can always make the LSEK almost an ideal low-pass filter so that the spectral accuracy is achieved by the LS method.

Fig. 17 indicates the dependence of the parameter M_h on Δt when $M = 33$. As one can see, when $\Delta t < 0.05$, the spectral accuracy is achieved and a small $M_h = 14$ is chosen because there is only one wave in the whole domain such that low degree Hermite polynomials are sufficiently good. When $\Delta t > 0.05$, the error grows up as Δt increases. It is reasonable because in this case the spatial bandwidth $\mathsf{r}_{\Delta t}$ is much larger than the computational support given by $M = 33$. It is noted that an even smaller M_h is chosen in this case. This can be explained from the dispersion analysis, Fig. 8. For a fixed M, a smaller M_h gives less oscillation in the low frequency part of the LSEK in the Fourier domain.

3.6. The Zakharov system

To demonstrate the reliability of the LSTS method and investigate the computational cost of this method, we consider the generalized Zakharov system (ZS), which can be described by the following equations [67]:

$$\mathrm{i}E_t + E_{xx} - \mathsf{a}NE = 0, \quad a < x < b, \ t > 0, \tag{74}$$

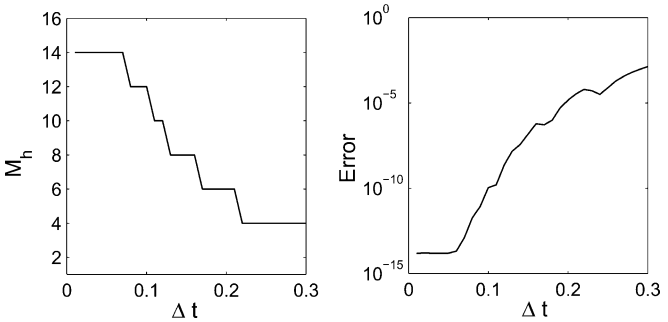

Fig. 17. Right figure: the dependence of the parameter M_h on Δt. Left figure: the changes of error in this case ; PPW = 4.65, $r = 3.05$, $M = 33$.

$$N_{tt} - (N - \mathbb{m}|E|^2)_{xx} = 0, \quad a < x < b, \ \ t > 0, \tag{75}$$

with

$$E(x,0) = E^0(x), \quad N(x,0) = N^0(x), \quad N_t(x,0) = N^{(1)}(x), \quad a \leqslant x \leqslant b, \tag{76}$$

$$E(a,t) = E(b,t), \quad E_x(a,t) = E_x(b,t), \quad t \geqslant 0, \tag{77}$$

$$N(a,t) = N(b,t), \quad N_x(a,t) = N_x(b,t), \quad t \geqslant 0. \tag{78}$$

In order to solve the problem, we split Eq. (74) into two equations,

$$\mathrm{i}E_t + 2E_{xx} = 0 \tag{79}$$

and

$$\mathrm{i}E_t = 2\mathsf{a}NE. \tag{80}$$

The first equation can be solved analytically by the LSEK. The second equation can be solved by integrating it from t to t', whose solution can be written as

$$E(x,t') = \exp\left(-\mathrm{i}\int_t^{t'} 2\mathsf{a}N(x,\mathsf{s})\,\mathrm{d}\mathsf{s}\right)E(x,t). \tag{81}$$

Similar to the FPTS method for the Zakharov system given in [67], the detailed second-order LSTS method from time $t = t_m$ to $t = t_{m+1}$ for the Zakharov system can be written as:

$$\frac{N^{m+1} - 2N^m + N^{m-1}}{\Delta t^2} = D_{xx}\left(N^m - \mathbb{m}|E^m|^2\right), \tag{82}$$

$$E^*(x_j) = \sum_{k=-M}^{M} K_{h,\mathsf{r}}\left(kh, \frac{1}{4}\Delta t\right)E^m(x_j - kh), \tag{83}$$

$$E^{**} = \exp\left(-\mathrm{i}\frac{\Delta t}{2}2\mathsf{a}(N^m + N^{m+1})/2\right)E^*, \tag{84}$$

$$E^{m+1}(x_j) = \sum_{k=-M}^{M} K_{h,\mathsf{r}}\left(kh, \frac{1}{4}\Delta t\right)E^{**}(x_j - kh), \tag{85}$$

where D_{xx} is defined as

$$D_{xx}f(x_j) = \sum_{k=-M}^{M} \mathsf{d}^{(2)}_{h,\mathsf{r}}(kh)f(x_j - kh), \tag{86}$$

with $\mathsf{d}^{(2)}_{h,\mathsf{r}}(kh)$ is given by Eq. (14). In fact, Jin et al. [31] proposed a better approach for integrating Eq. (75). However, the detail of their scheme is beyond the scope of the present work.

Example 1. We choose $\mathsf{a} = 1$ and $\mathbb{m} = -1$. The well-known solitary-wave solution of the ZS in this case is

$$E(x,t) = \sqrt{2B^2(1-C^2)}\,\mathrm{sech}(B(x - Ct))\mathrm{e}^{\mathrm{i}[(C/2)x - ((C/2)^2 - B^2)t]}, \tag{87}$$

$$N(x,t) = -2B^2\mathrm{sech}^2(B(x - Ct)), \quad -\infty < x < \infty, \ \ t \geqslant 0, \tag{88}$$

where B and C are constants. The initial condition is taken as

$$E^0(x) = E(x,0), \quad N^0(x) = N(x,0). \tag{89}$$

In our computation, we choose $B = 1$, $C = 0.5$. We solve the problem in the interval $[-32, 32]$ with periodic boundary conditions. Table 7 shows the numerical error of the FPTS and LSTS methods at time $t = 2$ with different mesh size h and step size Δt. It is obvious that the LSTS and FPTS methods achieve almost the same accuracy under the same discretization strategy and boundary conditions. The only difference is that when the mesh size h is larger, the accuracy of the FPTS method goes to 10^{-8} as Δt decreases, which is slightly higher than that of the LSTS method. However, when the mesh size h is fine enough, the LSTS method performs exactly as well as the FPTS method.

It is well known that the FFT can be computed in $O(N\log N)$ operations. The FPTS method employs the FFT, which makes the FPTS a computationally efficient method. The complexity of the LSTS method is $(2M + 1)N$ and scales as $O(N)$ at a fixed level of accuracy. Table 8 shows the comparison of the computing time needed by both the LSTS method and the FPTS method in solving the problem from time $t = 0$ to $t = 2$ under the periodic boundary condition. Note that the LSTS operates at the same spectral level of accuracy as that of the FPTS. Moreover, the periodic boundary condition is in favor of the FPTS. As one can see, the computing time required by the LSTS method is slightly larger than that of the FPTS method. However, the computing time of these two methods becomes closer and closer as the grid points N increases. Asymptotically, the LSTS method could require less computing time than the FPTS method does. For problems that does not require spectral accuracy, the LSTS method is much faster than the FPTS.

Since the time-splitting method is time reversible, we also investigate the time backward propagation process for both methods. The numerical error of both methods for this case is listed in Table 9. As one

Table 7
Error analysis of the FPTS and LSTS methods in the Zakharov system at time $t = 2$ in Example 1 in Section 3.6

	Δt	L_2			
		$h = \frac{1}{4}$		$h = \frac{1}{8}$	
		E	N	E	N
FPTS	0.1	5.153E − 3	1.113E − 2	5.152E − 3	1.116E − 2
	0.01	4.839E − 5	1.035E − 4	4.839E − 5	1.034E − 4
	0.0025	3.024E − 6	6.459E − 6	3.024E − 6	6.459E − 6
	0.000625	1.890E − 7	4.043E − 7	1.890E − 7	4.037E − 7
	0.00015625	1.199E − 8	3.345E − 8	1.180E − 8	2.524E − 8
LSTS	0.1	5.153E − 3	1.113E − 2	5.864E − 3	1.105E − 2
	0.01	4.839E − 5	1.034E − 4	4.839E − 5	1.034E − 4
	0.0025	3.024E − 6	6.459E − 6	3.024E − 6	6.459E − 6
	0.000625	2.180E − 7	4.753E − 7	1.890E − 7	4.037E − 7
	0.00015625	2.371E − 7	6.052E − 7	1.180E − 8	2.523E − 8

Table 8
Comparison of computing time of the FPTS and LSTS methods in the Zakharov system at time $t = 2$; $\Delta t = 0.000625$ in Example 1 in Section 3.6

	Computing time					
	$h = \frac{1}{4}$	$h = \frac{1}{8}$	$h = \frac{1}{16}$	$h = \frac{1}{32}$	$h = \frac{1}{64}$	$h = \frac{1}{128}$
FPTS	4.844s	9.875s	21.109s	44.016s	92.875s	200.656s
LSTS	6.844s	13.484s	26.938s	55.186s	108.356s	219.75s
g	29.2%	26.8%	21.5%	20.2%	14.3%	8.7%

Here $g = \frac{|t_2 - t_1|}{t_2} * 100\%$, where t_1 represents the computing time of the FPTS, t_2 represents the computing time of the LSTS.

Table 9
Error analysis of the FPTS and LSTS methods for time backward propagation in the Zakharov system at time $t = 0$ in Example 1 in Section 3.6

	Δt	L_2			
		$h = \frac{1}{4}$		$h = \frac{1}{8}$	
		E	N	E	N
Backward FPTS	0.1	5.153E − 3	1.113E − 2	5.153E − 3	1.127E − 2
	0.01	4.839E − 5	1.034E − 4	4.839E − 5	1.034E − 4
	0.0025	3.024E − 6	6.459E − 6	3.024E − 6	6.459E − 6
	0.000625	1.890E − 7	4.042E − 7	1.890E − 7	4.037E − 7
	0.00015625	1.200E − 8	3.345E − 8	1.180E − 8	2.524E − 8
Backward LSTS	0.1	5.153E − 3	1.113E − 2	9.663E − 3	1.145E − 2
	0.01	4.839E − 5	1.034E − 4	4.839E − 5	1.034E − 4
	0.0025	3.024E − 6	6.459E − 6	3.024E − 6	6.459E − 6
	0.000625	2.164E − 7	4.643E − 7	1.890E − 7	4.037E − 7
	0.00015625	2.352E − 7	5.645E − 7	1.180E − 8	2.523E − 8

The initial condition is taken as the exact solution of this system when $t = 2$.

can see, the backward propagation of the LSTS method is as efficient as the forward propagation of the LSTS method. It is competitive with the backward propagation of the FPTS method.

Example 2. The standard ZS with a plane-wave solution is considered. We choose $\mathsf{a} = 1$ and $\mathbb{m} = -1$ and consider the problem on the interval $[0, 2\pi]$. The initial condition is taken as

$$E^0(x) = \mathrm{e}^{\mathrm{i}7x}, \quad N^0(x) = 1, \quad N_t(x,0) = 0, \quad 0 \leqslant x \leqslant 2\pi. \tag{90}$$

The plane wave solution is

$$E(x,t) = \mathrm{e}^{\mathrm{i}(7x - \mathsf{x}t)}, \tag{91}$$

$$N(x,t) = 1, \quad 0 \leqslant x \leqslant 2\pi, \ \ t \geqslant 0, \tag{92}$$

with $\mathsf{x} = 50$.

We solve this problem by the LSTS method. A total of 256 grid points are used on the interval $[0, 26\pi]$ (i.e., 19 grid points in the interval $[0, 2\pi]$). Fig. 18 shows the numerical solution of Example 2. It is seen that by using only 2.71PPW, the numerical solution agrees with the exact plane wave solution extremely well.

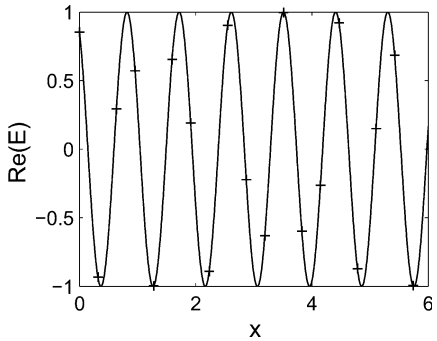

Fig. 18. The real part of E at $t = 2$ in Example 1 in Section 3.6. Solid line: exact solution given in Eq. (91); '+++': numerical solution.

3.7. Linear harmonic oscillator

To investigate the performance of high-order LSTS methods, we consider a linear Harmonic oscillator, which is described by the following Schrödinger equation:

$$\mathrm{i}\frac{\partial \mathsf{w}}{\partial t} = -\frac{1}{2}\frac{\partial^2 \mathsf{w}}{\partial x^2} + \frac{\mathsf{x}^2 x^2}{2}\mathsf{w}. \tag{93}$$

The ground state of the harmonic oscillator is

$$I(x) = \left(\frac{\mathsf{x}}{\pi}\right)^{1/4} \exp\left(-\frac{\mathsf{x}x^2}{2}\right). \tag{94}$$

The lowest energy of the harmonic oscillator is $E_0 = (1/2)\mathsf{x}$, thus

$$\mathsf{w}(x,t) = \exp(-\mathrm{i}E_0 t)\, I(x) \tag{95}$$

is an exact solution of Eq. (93). In order to solve the problem, we split Eq. (93) into two equations:

$$\mathrm{i}\frac{\partial \mathsf{w}}{\partial t} = -\frac{\partial^2 \mathsf{w}}{\partial x^2}, \tag{96}$$

$$\mathrm{i}\frac{\partial \mathsf{w}}{\partial t} = \mathsf{x}^2 x^2 \mathsf{w}. \tag{97}$$

The first one can be solved by the LSEK analytically and the second one can be integrated analytically from time t to t'

$$\mathsf{w}(x,t) = \exp\left(-\mathrm{i}(t-t')\mathsf{x}^2 x^2\right)\mathsf{w}(x,t'). \tag{98}$$

By alternatively solving these two equations in 2, 3 and 7 split steps, one obtains the first-, second- and fourth-order LSTS method. We also solve this problem by the FPTS method to compare the accuracy of both methods. In our computation, a sufficiently large interval $[-30, 30]$ is chosen. Two hundred and fifty six grid points are used for this interval, i.e., $N = 256$. The initial condition is taken as the solution of this system, when $t = 0$. Periodic boundary condition is used for both methods. The numerical solutions are compared with the exact solutions at $t = 1$.

Table 10 shows the error analysis for the linear harmonic oscillator. It is noted that high accuracy can be achieved by using high-order time-splitting methods. Smaller step size Δt can also achieve higher accuracy. The LSTS method can give the same order of accuracy as the FPTS method does under the same discretization strategy.

Table 10
Errors analysis for linear harmonic oscillator in Section 3.7

Method	Step size	FPTS		LSTS	
		L_∞	L_2	L_∞	L_2
First-order	$\Delta t = 0.01$	1.803E − 3	2.975E − 3	1.795E − 3	2.975E − 3
	$\Delta t = 0.001$	1.803E − 4	2.975E − 4	1.795E − 4	2.975E − 4
Second-order	$\Delta t = 0.01$	4.740E − 6	7.724E − 6	4.717E − 6	7.724E − 6
	$\Delta t = 0.001$	4.740E − 8	7.724E − 8	4.717E − 8	7.724E − 8
Fourth-order	$\Delta t = 0.01$	2.095E − 10	4.007E − 10	2.095E − 10	4.007E − 10
	$\Delta t = 0.001$	3.586E − 13	6.180E − 13	2.418E − 13	4.685E − 13

4. Application

In this section, the LSTS method is applied to Fishers' equation, the generalized nonlinear Schrödinger equation, the ground state and the time evolution of Bose–Einstein condensates and the nonlinear Schrödinger equations in semi-classical regime. The FPTS method is employed for a comparison.

4.1. Fisher's equation

Fisher's equation was introduced to represent the evolution of the population due to diffusion and nonlinear local multiplication [84]. The 1D nonlinear parabolic partial differential equation, which describes the kinetic advancing rate of an advantageous gene, can be written as

$$\frac{\partial u}{\partial t} = \mathsf{l}\frac{\partial^2 u}{\partial x^2} + \mathsf{q}u(1-u), \quad x \in (-\infty, \infty), \ \ t > 0, \tag{99}$$

where the positive quantities l and q are the diffusion coefficient and the reaction factor, respectively. Eq. (99) also provides a prototype model for a spreading flame [85] and a model equation for the finite domain evolution of neutron population in a nuclear reactor [86].

By use of the transformation $x := (1/\mathsf{l})^{1/2}x$, Fisher's equation returns a simpler form

$$\frac{\partial u}{\partial t} = \frac{\partial^2 u}{\partial x^2} + \mathsf{q}u(1-u). \tag{100}$$

The non-local initial and boundary conditions for Fisher's equation are given as

$$u(x,0) = u_0(x) \in [0,1], \quad x \in (-\infty, \infty), \tag{101}$$

$$\lim_{x\to-\infty} u(x,t) = 1, \quad \lim_{x\to\infty} u(x,t) = 0, \tag{102}$$

with the x derivative tending to zero as $x \to \pm\infty$ and the assumption that the saturation level is unity.

Properties of Fisher's equation have been studied theoretically by many authors, including Fisher [84], Kolmogorov et al. [85], Canosa [86], Larson [87], Hagan [88], etc. For the non-local conditions, it is proved that there is a traveling wave solution to Eq. (99) with a wave speed c. Because the accurate and reliable numerical representation of the traveling wave solution to Fisher's equation is an interesting and challenging numerical problem, the traveling wave solution of Fisher's equation has also been studied numerically by many researchers, using the method of accurate space derivatives (ASD) [90], finite differences [89], finite elements [91], the DSC [54], as well as many others [92,93].

The superspeed wave solution [92] satisfying Eq. (99) is employed in the present numerical study

$$u(x,t) = \left[1 + \exp\left(\sqrt{\frac{\mathsf{q}}{6}}x - \frac{5\mathsf{q}}{6}t\right)\right]^{-2}. \tag{103}$$

The non-local boundary conditions, which are commonly used in the literature [90,91], are given as

$$u(x_{\mathrm{L}}, t) = 1, \quad u(x_{\mathrm{R}}, t) = 0. \tag{104}$$

In order to solve the problem by the LSTS method, Fisher's equation is split into two equations:

$$\frac{\partial u}{\partial t} = 2\frac{\partial^2 u}{\partial x^2} + 2\mathsf{q}u \tag{105}$$

and

$$\frac{\partial u}{\partial t} = -2\mathsf{q}u^2. \tag{106}$$

The first equation can be solved by the LSEK analytically. The second equation can be integrated from time t_0 to time t analytically

$$u(x,t) = \frac{u(x,t_0)}{1 + 2\mathsf{q}(t-t_0)u(x,t)}. \tag{107}$$

Fourth-order time-splitting method is used in the present local spectral method in our computation. We consider $\mathsf{q} = 1$ in solution (103). The computational domain is chosen to be sufficiently large [−64, 64]. In order to compare with other methods, the fourth-order Runge–Kutta (RK4) is used for the DSC and Fourier pseudospectral method (FP) methods. A detailed comparison of the LSTS, DSC-RK4, Crank–Nicolson finite difference (CNFD), FP-RK4 is given in Table 11. It can be seen that the LSTS method always has accuracy comparable to the DSC-RK4 and FP-RK4 methods, and these three schemes achieve very high accuracy.

The mesh strategies in Table 11 are specially designed [54]. First, in order to test the temporal accuracy order, the spatial resolution is chosen as sufficiently fine and kept unchanged. For high-order methods, such as the LSTS, the DSC-RK4 and the FP-RK4, $\Delta x = 1.0$ is fine enough. While for CNFD method, Δx is set to be 0.25 since the second-order finite difference scheme is used for spatial discretization in this method. In addition, Δx could not be too small for three explicit schemes, the DSC-RK4, FP-RK4 and ASD, because of the stability constraint for the mesh ratio $\Delta t/\Delta x$. However, the present LSTS method is both explicit and unconditionally stable so that stable numerical solutions can still be obtained when $\Delta x = 0.25$ and $\Delta t = 0.2$,

Table 11
Numerical errors in solving a scaled Fisher's equation by using the LSTS, DSC-RK4, CNFD, FP-RK4, and ASD

Scheme	Δx	Δt	$t = 5.0$		$t = 10.0$	
			L_∞	L_2	L_∞	L_2
LSTS	0.25	0.2	2.22E − 6	7.46E − 6	2.28E − 6	7.91E − 6
	1.0	0.2	2.21E − 6	7.47E − 6	2.28E − 6	7.92E − 6
	1.0	0.1	1.39E − 7	4.68E − 7	1.43E − 7	4.96E − 7
	2.0	0.01	3.62E − 5	1.31E − 4	3.89E − 5	1.51E − 4
	1.0	0.01	2.35E − 9	6.24E − 9	2.73E − 9	6.65E − 9
DSC-RK4	1.0	0.2	1.34E − 5	2.74E − 6	5.61E − 5	1.17E − 5
	1.0	0.1	9.00E − 7	1.84E − 7	3.86E − 6	8.03E − 7
	2.0	0.01	4.35E − 6	9.38E − 7	3.12E − 6	6.50E − 7
	1.0	0.01	1.59E − 9	2.50E − 10	1.39E − 9	2.06E − 10
FP-RK4	1.0	0.2	1.34E − 5	2.74E − 5	5.61E − 5	1.17E − 5
	1.0	0.1	9.01E − 7	1.84E − 7	3.86E − 6	8.03E − 7
	2.0	0.01	3.16E − 6	6.75E − 7	3.21E − 6	6.76E − 7
	1.0	0.01	1.27E − 9	1.38E − 10	4.40E − 10	8.78E − 11
CNFD	0.25	0.2	5.18E − 3	1.10E − 3	1.43E − 2	2.99E − 3
	0.25	0.1	1.35E − 3	2.91E − 4	4.25E − 3	8.88E − 4
	2.0	0.01	1.02E − 2	1.87E − 3	5.47E − 2	1.16E − 2
	1.0	0.01	2.66E − 3	4.84E − 2	1.46E − 2	3.06E − 3
ASD	1.0	0.2	3.84E − 2	7.24E − 3	1.09E − 1	2.19E − 2
	1.0	0.1	1.96E − 2	3.73E − 3	5.62E − 2	1.14E − 2
	2.0	0.01	1.99E − 3	3.83E − 4	5.67E − 3	1.18E − 3
	1.0	0.01	1.99E − 3	3.83E − 4	5.72E − 3	1.18E − 3

which is the same mesh strategy used for the CNFD method. Second, we choose a sufficiently fine temporal resolution, i.e., $\Delta t = 0.01$, and keep it unchanged to test the spatial accuracy order.

In terms of the L_2 error, the error decreasing rates of each scheme are recalculated from Table 11 and are presented in Table 12. The numerical results indicate that the spatial accuracy order of the LSTS method is extremely high and comparable with the DSC-RK4 and FP-RK4 methods. The temporal discretization orders of the LSTS, DSC-RK4 and FP-RK4 are all approximately $O(\Delta t^4)$. The spatial and temporal accuracy orders of the CNFD method are of $O(\Delta x^2)$ and $O(\Delta t^2)$, respectively. For the ADS method, the approximation errors are introduced fully by temporal discretization and the temporal accuracy order is of $O(\Delta t)$, see Ref. [54] for more details.

4.2. The generalized nonlinear Schrödinger equation

The nonlinear Schrödinger equations (NLS) has important applications in fluid dynamics, nonlinear optics, and plasma physics. It has been investigated analytically and numerically by many authors [94–97]. The generalized nonlinear Schrödinger equation can be written as

$$\mathrm{i}u_t - u_{xx} + q(|u|^2)u = 0, \quad x \in [x_\mathrm{L}, x_\mathrm{R}], \ \ t > 0, \tag{108}$$

$$u|_{x=x_\mathrm{L}} = 0, \quad u|_{x=x_\mathrm{R}} = 0, \tag{109}$$

where $q(s)$ can be chosen as $q(s) = s_\mathrm{p}$, $p > 0$, $q(s) = s/(1 + s)$ or $q(s) = \ln(1 + s)$ in different physical problems.

In order to solve this problem, we split Eq. (108) into two parts:

$$\mathrm{i}u_t = 2u_{xx} \tag{110}$$

and

$$\mathrm{i}u_t = -2q(|u|^2)u. \tag{111}$$

The first equation can be solved analytically by the LSEK. To solve the second one, multiplying it by $\overline{u}$, the conjugate of u, one obtains

$$\mathrm{i}u_t\overline{u} = -2q(|u|^2)|u|^2. \tag{112}$$

Subtracting the conjugate of Eq. (112) from Eq. (112) and multiplying by $-\mathrm{i}$, one obtains

$$\frac{\mathrm{d}}{\mathrm{d}t}|u|^2 = 0. \tag{113}$$

Therefore, $|u|^2$ is independent of time in the second equation from time t to t', whose solution can be written as

$$u(x, t') = \exp\left(2\mathrm{i}(t' - t)q(|u(x, t)|^2)\right)u(x, t). \tag{114}$$

Table 12
Numerically tested accuracy order of the four methods

Time	Halve	LSTS	DSC-RK4	Scheme FP-RK4	FDCN	ASD
$t = 5.0$	Δt	3.99	3.89	3.894	1.92	0.96
	Δx	14.36	11.87	12.26	1.95	3.77E − 5
$t = 10.0$	Δt	4.00	3.86	3.86	1.75	0.94
	Δx	14.47	11.62	12.91	1.92	1.22E − 4

By alternatively solving the above two equations in several split steps, one can solve Eq. (108) from time t_m to t_{m+1} by the LSTS method.

Example 1. The cubic Schrödinger equation

1. *One-soliton solution*. First, we consider the initial-value problem

$$\mathrm{i}u_t - u_{xx} - 2|u|^2 u = 0, \quad t > 0, \tag{115}$$

$$u|_{t=0} = u_0(x) = \operatorname{sech}(x+2)\exp[-2\mathrm{i}(x+2)]. \tag{116}$$

The exact solution is

$$u(x,t) = \operatorname{sech}(x+2-4t)\exp[-\mathrm{i}(2x+4-3t)]. \tag{117}$$

In our computation, a sufficiently large interval $[-20, 20]$ is chosen and $N = 256$. The step size Δt is 0.01. The soliton solution is computed from $t = 0$ to $t = 1$. We solve this problem by both the LSTS and FPTS methods. The first-, second- and fourth-order splitting schemes are adopted in both methods. To compare the results, periodic boundary condition is used in both methods. Fig. 19 shows the propagation of the solitary wave in this problem. Table 13 shows the L_∞ and L_2 errors of the numerical solutions with respect to the exact solutions for both methods. As we can see, the LSTS and FPTS give exactly the same accuracy.

2. *Collision of two solitons*. Second, we consider interacting solitons for the cubic Schrödinger equation (115) with the initial condition

$$u|_{t=0} = u_0(x) = \operatorname{sech}(x-10)\exp[-\mathrm{i}(2x-20)] \tag{118}$$

$$+ \operatorname{sech}(x+10)\exp[\mathrm{i}(2x+20)]. \tag{119}$$

The exact solution of the initial-value problem (115) and (119) is

$$u(x,t) = \operatorname{sech}(x-10+20t)\exp[-\mathrm{i}(2x-20-3t)] + \operatorname{sech}(x+10-20t)\exp[\mathrm{i}(2x+20+3t)]. \tag{120}$$

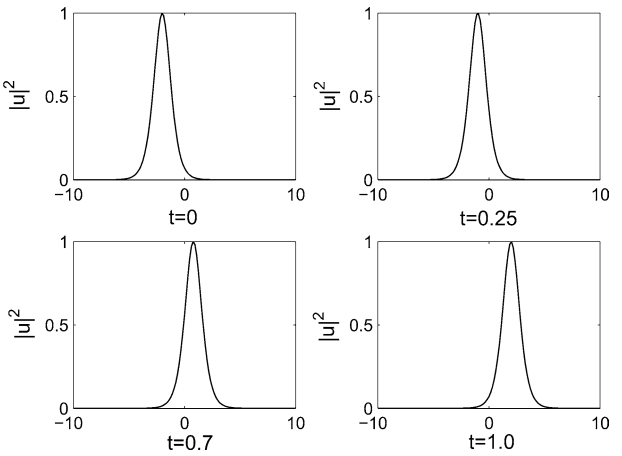

Fig. 19. LSTS solutions at different times for Example 1 in Section 4.2.

Table 13
Errors analysis for Example 1.1 in Section 4.2

Method		L_∞	L_2
FPTS	First-order	4.049E − 3	8.060E − 3
	Second-order	8.922E − 5	1.093E − 4
	Fourth-order	2.703E − 7	3.435E − 7
LSTS	First-order	4.049E − 3	8.060E − 3
	Second-order	8.922E − 5	1.093E − 4
	Fourth-order	2.703E − 7	3.435E − 7

In our computation, a sufficiently large interval $[-20, 20]$ is chosen and $N = 256$. The step size Δt is 0.01. The soliton solution is computed from $t = 0$ to $t = 1$. In order to compare the results, the periodic boundary condition is used in both the LSTS and FPTS methods. Fig. 20 shows the interaction of two solitary wave in this problem. As one can see, the two waves move in the opposite directions. After their interaction, both the solitary waves keep their original shapes and velocities. Our numerical results are consistent with the wave interaction theory. Table 14 shows the L_∞ and L_2 errors of the numerical solutions by both the FPTS and LSTS methods. It is noted that exactly the same accuracy is achieved again by the LSTS and FPTS methods.

Example 2. Plane wave soliton for the GNLS equation

$$iu_t - u_{xx} + q(|u|^2)u = 0, \tag{121}$$

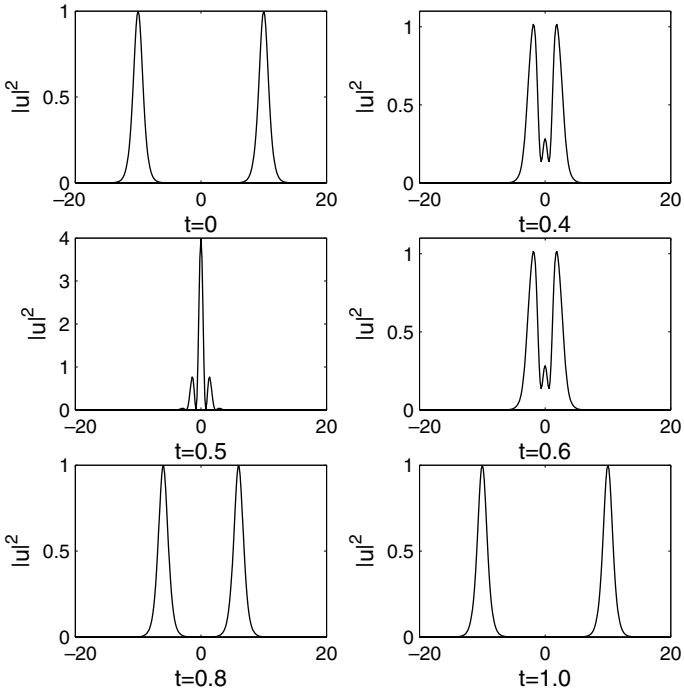

Fig. 20. LSTS solutions at different times for Example 2 in Section 4.2.

Table 14
Errors analysis for Example 1.2 in Section 4.2

Method		L_∞	L_2
FPTS	First-order	4.054E − 3	1.140E − 2
	Second-order	8.838E − 5	1.546E − 4
	Fourth-order	2.671E − 7	4.852E − 7
LSTS	First-order	4.054E − 3	1.140E − 2
	Second-order	8.838E − 5	1.546E − 4
	Fourth-order	2.671E − 7	4.852E − 7

$$u(x+L) = u(x). \tag{122}$$

The problem admits a progressive plane wave solution

$$u(x,t) = A\exp[\mathrm{i}(kx - \mathrm{x}t)], \tag{123}$$

with $w = -k^2 - q(A^2)$. In our computation, we set $A = 2, k = \pi$, $L = 2$. The mesh size is $h = 0.3125$ and the step size is $\Delta t = 0.01$. The plane wave solution is computed from $t = 0$ to $t = 2\pi/|\mathrm{x}|$ on interval $[0, 20L]$. The periodic boundary condition is used in both methods. Table 15 shows the L_∞ and L_2 errors of the numerical solutions by both the FPTS and LSTS methods. As one can see, very high accuracy has been achieved even when the first-order time-splitting method is used. The FPTS method performs slightly better than the LSTS method does in this case because the plane wave solution is band limited in the Fourier domain, which is the most suitable kind of functions to be approximated by the FP method.

4.3. The ground state solution of Bose–Einstein condensates

Since the first experimental realization of Bose–Einstein condensates (BECs), there has been a great deal of work which theoretically and numerically describes the single particle properties of BECs by using the

Table 15
Errors analysis for Example 2 in Section 4.2

Method		$q(S)$	L_∞	L_2
FPTS	First-order	S^2	6.167E − 14	1.616E − 13
		$-\frac{4S}{S+1}$	3.496E − 14	8.473E − 14
		$\ln(1+S)$	3.537E − 14	9.031E − 14
	Second-order	S^2	1.870E − 14	3.794E − 14
		$-\frac{4S}{S+1}$	3.406E − 14	8.516E − 14
		$\ln(1+S)$	3.350E − 14	9.086E − 14
	Fourth-order	S^2	1.984E − 12	1.858E − 12
		$-\frac{4S}{S+1}$	4.740E − 14	1.561E − 13
		$\ln(1+S)$	3.983E − 14	1.150E − 13
LSTS	First-order	S^2	4.453E − 14	1.359E − 13
		$-\frac{4S}{S+1}$	4.883E − 14	1.540E − 13
		$\ln(1+S)$	4.903E − 14	9.318E − 14
	Second-order	S^2	4.703E − 14	1.056E − 14
		$-\frac{4S}{S+1}$	5.604E − 14	1.550E − 13
		$\ln(1+S)$	4.561E − 14	1.018E − 14
	Fourth-order	S^2	1.254E − 12	7.637E − 12
		$-\frac{4S}{S+1}$	4.550E − 13	2.760E − 12
		$\ln(1+S)$	6.311E − 13	3.900E − 12

Gross–Pitaevskii equation (GPE) [98,99]. The interaction of particles is described by a mean field which leads to a nonlinear term in the GPE. The results obtained from the GPE show good agreement with the experiments [100–102]. One of the fundamental problems in the BEC is to find the ground state solution of the GPE. The numerical study of the ground state of the GPE has been of interest to many authors [33,103,104] in recent years.

We consider the following dimensionless Gross–Pitaevskii equation under the normalization in three spatial dimensions:

$$\mathrm{i}\frac{\partial \mathsf{w}}{\partial t} = -\frac{1}{2}\Delta \mathsf{w} + V(\mathbf{x})\mathsf{w} + \mathsf{b}|\mathsf{w}|^2\mathsf{w}, \quad \mathbf{x} \in \mathsf{X}, \ \ t > 0, \tag{124}$$

$$\mathsf{w}(\mathbf{x}, t) = 0, \quad \mathbf{x} \in \mathsf{C} = \partial\mathsf{X}, \quad t \geqslant 0, \tag{125}$$

where

$$V(x) = \tfrac{1}{2}(\mathsf{c}_x^2 x^2 + \mathsf{c}_y^2 y^2 + \mathsf{c}_z^2 z^2). \tag{126}$$

An important invariant of Eq. (124) is the energy

$$E_{\mathsf{b}}(\mathsf{w}) = \int_{\mathsf{X}} \left[\frac{1}{2}|\nabla \mathsf{w}(\mathbf{x}, t)|^2 + V(\mathbf{x})|\mathsf{w}(\mathbf{x}, t)|^2 + \frac{\mathsf{b}}{2}|\mathsf{w}(\mathbf{x}, t)|^4\right] \mathrm{d}\mathbf{x}, \quad t \geqslant 0. \tag{127}$$

To find the ground state of Eq. (124), we write

$$\mathsf{w}(\mathbf{x}, t) = \mathrm{e}^{-\mathrm{i}\mathsf{l}t} \mathsf{f}(\mathbf{x}), \tag{128}$$

where l is the chemical potential of the condensate and f satisfies the following equation:

$$\mathsf{l}\,\mathsf{f}(\mathbf{x}) = -\tfrac{1}{2}\Delta \mathsf{f}(\mathbf{x}) + V(\mathbf{x})\mathsf{f}(\mathbf{x}) + \mathsf{b}|\mathsf{f}(\mathbf{x})|^2 \mathsf{f}(\mathbf{x}), \quad \mathbf{x} \in \mathsf{X}, \tag{129}$$

$$\mathsf{f}(\mathbf{x}) = 0, \quad \mathbf{x} \in \mathsf{C}, \tag{130}$$

with normalization condition

$$\int_{\mathsf{X}} |\mathsf{f}(\mathbf{x})|^2 \, \mathrm{d}\mathbf{x} = 1. \tag{131}$$

This is an eigenvalue problem and the eigenvalue is given by

$$\mathsf{l} = E_{\mathsf{b}}(\mathsf{f}) + \int_{\mathsf{X}} \frac{\mathsf{b}}{2}|\mathsf{f}(\mathbf{x})|^4 \, \mathrm{d}\mathbf{x}. \tag{132}$$

The non-rotating BEC ground state solution $\mathsf{f}_{\mathsf{g}}(\mathbf{x})$ is a real non-negative function found by minimizing the energy $E_{\mathsf{g}}(\mathsf{f})$ under the constraint (129) [105]. To compute the minimizer of the energy functional $E_{\mathsf{b}}(\mathsf{f})$, it is natural to adapt the following splitting scheme, which was widely used in the physics literature [104,106,107] for computing the ground state solution of BECs:

$$\begin{aligned} \mathsf{f}_t &= -\frac{1}{2}\frac{\mathrm{d}E_{\mathsf{b}}(\mathsf{f})}{\mathrm{d}\mathsf{f}} \\ &= \tfrac{1}{2}\Delta \mathsf{f} - V(\mathbf{x})\mathsf{f} - \mathsf{b}|\mathsf{f}|^2\mathsf{f}, \quad \mathbf{x} \in \mathsf{X}, \ \ t_n < t < t_{n+1}, n \geqslant 0, \end{aligned} \tag{133}$$

$$\mathsf{f}(\mathbf{x}, t_{n+1}) = \mathsf{f}(\mathbf{x}, t_{n+1}^+) = \frac{\mathsf{f}(\mathbf{x}, t_{n+1}^-)}{\|\mathsf{f}(\cdot, t_{n+1}^-)\|}, \tag{134}$$

$$\mathsf{f}(\mathbf{x}, t) = 0, \quad \mathbf{x} \in \mathsf{C}, \tag{135}$$

where we denote $\|\cdot\| = \|\cdot\|_{\mathrm{L2}(\mathsf{X})}$.

In fact, the above algorithm can be viewed as firstly applying the steepest decent method to the energy functional $E_{\mathsf{b}}(\phi)$ without constraint by Eq. (133), then projecting the solution back to the unit sphere by Eq. (134) in order to satisfy the normalization condition.

For $d = 1$, we have

$$\phi_t = \tfrac{1}{2}\phi_{xx} - V(x)\phi - \mathsf{b}|\phi|^2\phi, \quad x \in \mathsf{X} = (a,b), \ \ t_n < t < t_{n+1}, \ \ n \geqslant 0, \tag{136}$$

$$\phi(x,t_{n+1}) = \phi(x,t_{n+1}^+) = \frac{\phi(x,t_{n+1}^-)}{\|\phi(\cdot,t_{n+1}^-)\|}, \tag{137}$$

$$\phi(a,t) = \phi(b,t) = 0, \quad t \geqslant 0. \tag{138}$$

In order to solve the problem by the second-order LSTS method from time t_m to time t_{m+1}, Eqs. (136) and (137) are solved in four steps. First, one solves

$$\phi_t(x,t) = -2V(x)\phi(x,t) - 2\mathsf{b}|\phi|^2\phi(x,t) \tag{139}$$

from time t_m to $t_m + \frac{1}{4}\Delta t$. The solution of Eq. (139) is given by Bao and Du [33]

$$\phi(x,t) = \begin{cases} \sqrt{\dfrac{V(x)e^{-2V(x)(t-t_m)}}{V(x)+\mathsf{b}(1-e^{-2V(x)(t-t_m)})|\phi|^2}}\,\phi(x,t_m), & V(x) \neq 0, \\ \sqrt{\dfrac{1}{1+4\mathsf{b}(t-t_m)|\phi|^2}}\,\phi(x,t_m), & V(x) = 0. \end{cases} \tag{140}$$

Then one solves

$$\phi_t = \phi_{xx} \tag{141}$$

analytically by the LSEK from time $t_m + \frac{1}{4}\Delta t$ to $t_m + \frac{3}{4}\Delta t$, followed by solving Eq. (139) from time $t_m + \frac{3}{4}\Delta t$ to t_{m+1}. Finally, one let

$$\phi(x,t_{m+1}) = \frac{\phi^*(x,t_{m+1})}{\|\phi^*(x,t_{m+1})\|}, \tag{142}$$

where $\phi^*(x, t_{m+1})$ is the value calculated from the previous step.

Example 1. We consider two cases:

1. The linear case ($\mathsf{b} = 0$) with a double-well potential,

$$V(x) = \frac{1}{2}(1-x^2)^2, \quad \mathsf{b} = 0, \ \phi_0(x) = \frac{1}{(4\pi)^{1/4}}e^{-x^2/8}, \quad x \in R. \tag{143}$$

2. A nonlinear case ($\mathsf{b} > 0$) with a harmonic oscillator potential,

$$V(x) = \frac{x^2}{2}, \quad \mathsf{b} = 60, \quad \phi_0(x) = \frac{1}{(\pi)^{1/4}}e^{-x^2/2}, \quad x \in R. \tag{144}$$

Cases 1 and 2 are solved, respectively, on $[-16, 16]$ and $[-8, 8]$ with a mesh size $h = 1/32$. We solve the problems by both the LSTS and FPTS methods with periodic boundary conditions. Fig. 21 shows the evolution of the energy $E_{\mathsf{b}}(\phi)$ for different time steps Δt. As one can see, the LSTS and the FPTS give exactly the same result under the same time step in both cases. Even a larger time step is used, i.e., $\Delta t = 0.2$ in case 1 and $\Delta t = 0.05$ in case 2, the numerical results converge to the energy of the ground state.

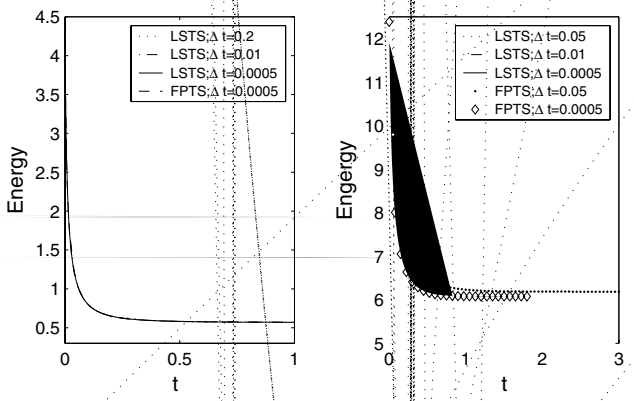

Fig. 21. Energy evolution for Example 1 in Section 4.3. Left figure for case 1. Right figure for case 2.

Example 2. Ground state solution of 1D BECs with harmonic oscillator potential

$$V(x) = \frac{x^2}{2}, \quad \phi_0(x) = \frac{1}{\pi^{1/4}} e^{-x^2/2}, \quad x \in R, \tag{145}$$

In our computations, the mesh size h is 1/8 and time step Δt is 0.001. The problem is solved in interval $[-16, 16]$ by both the FPTS and LSTS methods with periodic boundary condition. Fig. 22 shows the ground state solution $\phi_g(x)$ and energy evolution for different β. The result agrees very well with the solution obtained by Bao and Du [33].

Example 3. Ground state solution of BECs in 2D:

$$V(x, y) = \tfrac{1}{2}(\gamma_x^2 x^2 + \gamma_y^2 y^2). \tag{146}$$

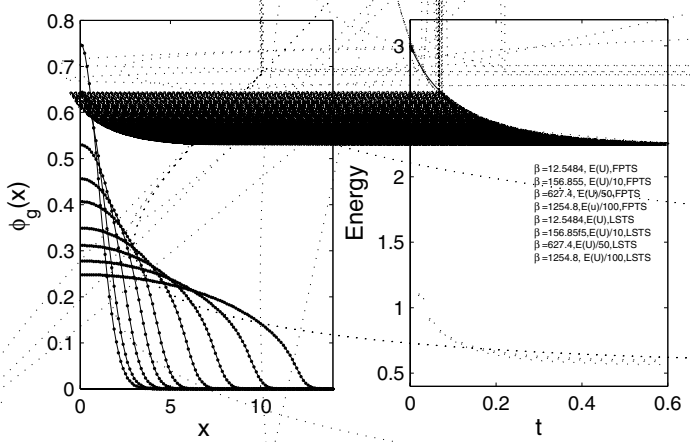

Fig. 22. Ground state solution ϕ_g for Example 2 in Section 4.3. Right figure: Energy evolution for different β. Left figure: For $\beta = 0$, 3.1371, 12.5484, 31.371, 62.724, 156.855, 313.71, 627.42, 1254.8 (with decreasing peak).

The initial condition is chosen as

$$\phi_0(x,y) = \frac{(\gamma_x\gamma_y)^{1/4}}{\pi^{1/2}} e^{-(\gamma_x x^2+\gamma_y y^2)/2}. \tag{147}$$

To quantify the ground state solution $\phi_g(x,y)$, we define the radius mean square

$$\alpha_{\rm rms} = \left\|\alpha\phi_g^2\right\|_{L^2(\Omega)} = \sqrt{\int_\Omega \alpha^2\phi_g^2(x,y)\,dx\,dy}. \tag{148}$$

In our computation, $\gamma_x = 1$, $\gamma_y = 4$, $\beta = 200$ and the problem is solved by the LSTS on $\Omega = [-8, 8]\times[-4, 4]$ with mesh size $h_x = 1/8$, $h_y = 1/16$ and step size $\Delta t = 0.001$. We obtain the following results from the ground state solution ϕ_g:

$$x_{\rm rms} = 2.2734, \quad y_{\rm rms} = 0.6074, \quad \phi_g^2(0,0) = 0.0808, \quad E_b(\phi_g) = 11.1563, \quad \mu_g = 16.3377.$$

These results are the same as those given by Bao and Du [33]. Fig. 23 shows the surface plot of the ground state solution ϕ_g.

4.4. The time evolution of Bose–Einstein condensation

To find the dynamics of a Bose–Einstein condensation, we consider the Gross–Pitaevskii equation given in Section 4.3

$$i\frac{\partial\psi}{\partial t} = -\frac{1}{2}\Delta\psi + V(\mathbf{x})\psi + \beta|\psi|^2\psi, \quad \mathbf{x}\in\Omega, \quad t > 0. \tag{149}$$

For the 1D case, we have

$$i\frac{\partial\psi}{\partial t} = -\frac{1}{2}\psi_{xx} + V(x)\psi + \beta|\psi|^2\psi, \quad x\in\Omega, \quad t > 0, \tag{150}$$

with $V(x) = \gamma^2x^2/2$.

We use both the FPTS and LSTS methods to solve Eq. (150), i.e., we integrate

$$i\frac{\partial\psi}{\partial t} = -\psi_{xx} \tag{151}$$

analytically by the LSEK in $(1/4)\Delta t$, before we solve

$$i\frac{\partial\psi}{\partial t} = 2V(x)\psi + 2\beta|\psi|^2\psi \tag{152}$$

in $(1/2)\Delta t$. Finally, we solve

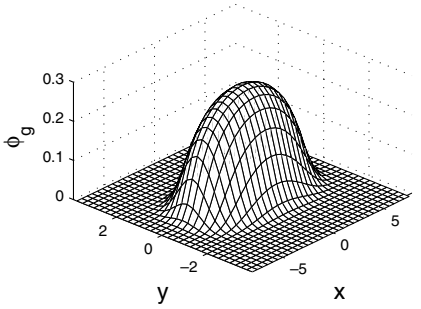

Fig. 23. Ground state solutions ϕ_g for Example 3 in Section 4.3.

$$\mathrm{i}\frac{\partial \mathsf{w}}{\partial t} = -\mathsf{w}_{xx} \tag{153}$$

in (1/4)Δt again. The initial condition $\mathsf{w}_0(x)$ is chosen as the ground state of the 1D GPE (150) with $\mathsf{c} = 1$ and $\mathsf{b} = 50$, which are obtained from Example 2 in Section 4.3.

In our computation, a sufficiently large interval $[-12, 12]$ is chosen and 1024 grids points are used on this interval. Step size Δt is 0.001. We let $\mathsf{c} = 2$ in Eq. (150) according to an experimental setup, where initially the condensate is assumed to be in its ground state, and the trap frequency is double at $t = 0$.

To quantify the numerical results, we define the condensate width

$$\mathsf{r}_x^2 = \int x^2 |\mathsf{w}(x,t)|\, \mathrm{d}x. \tag{154}$$

Fig. 24 shows the time evolution of central density and condensate width of the wavefunction. It is noted that the LSTS and FPTS methods give identical results for this problem, which are the same as the ones given in [32].

4.5. The Schrödinger equation in the semiclassical regime

The Schrödinger equation with a small (scaled Planck) constant ϵ can describe many problems in solid physics,

$$\epsilon u_t^\epsilon - \mathrm{i}\frac{\epsilon^2}{2}\Delta u^\epsilon + \mathrm{i}V(\mathbf{x})u^\epsilon = 0, \quad t \in R, \quad \mathbf{x} \in R^d, \tag{155}$$

where $V(\mathbf{x})$ is a given electrostatic potential, $0 < \epsilon \ll 1$. The position density can be computed by

$$n^\epsilon(\mathbf{x},t) = |u^\epsilon(\mathbf{x},t)|^2 \tag{156}$$

and the current density can be computed by

$$J^\epsilon(\mathbf{x},t) = \epsilon \mathrm{Im}(\overline{u^\epsilon(\mathbf{x},t)}\nabla u^\epsilon(\mathbf{x},t)) = \frac{1}{2\mathrm{i}}(\overline{u^\epsilon}\nabla u^\epsilon - u^\epsilon \nabla \overline{u^\epsilon}), \tag{157}$$

where " — " denotes complex conjugation.

It is well known that the convergence of u^ϵ as $\epsilon \to 0$ is not strong because Eq. (155) propagates oscillations of wavelength ϵ in space and time. The oscillatory nature of Eq. (155) provides several numerical burdens. In order to attain correct results of the position density and current density, one must fully resolve the

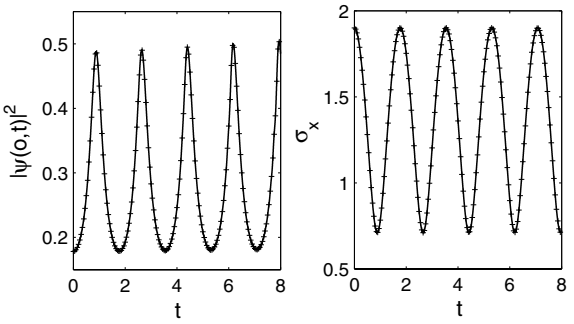

Fig. 24. Evolution of the central density and condensate width for the problem in Section 4.4. Solid lines represent the results by the LSTS. '+++' represents the results by the FPTS. Left figure: Central density $|\mathsf{w}(0,t)|^2$, the small figure inside is the amplifications of a part of the left figure; Right figure: Condensate width r_x.

spatial–temporal oscillations numerically, i.e., use many grid points per wavelength of O(ϵ). In Ref. [108], Markowich et al. show that the following constraint is needed to guarantee good approximations for small ϵ,

$$h = o(\epsilon), \quad \Delta t = o(\epsilon). \tag{158}$$

Bao et al. [34] employed the FPTS to solve this problem. Due to the exponentially high-order accuracy of spectral method, it allows the mesh size *one order of magnitude larger* than the finite difference method provided [108]. Bao et al. [34] prove that the mesh strategy

$$h = O(\epsilon), \quad \Delta t = o(\epsilon) \tag{159}$$

conserves the position density and gives a uniform L^2-approximation of the wavefunction. Nevertheless, they confirm that the correct results of the position and current densities can be obtained with much weaker constraints

$$h = O(\epsilon), \quad \Delta t = O(1). \tag{160}$$

In our computation, we use the LSTS method to solve Eq. (155) and compare our results with those of the FPTS and finite difference method. Our numerical results show that the same mesh strategy

$$h = O(\epsilon), \quad \Delta t = O(1) \tag{161}$$

works very well for the LSTS method.

For $d = 1$, the problem becomes

$$\epsilon u_t^\epsilon - \mathrm{i}\frac{\epsilon^2}{2} u_{xx}^\epsilon + \mathrm{i}V(x)u^\epsilon = 0, \quad a < x < b, \ \ t > 0, \tag{162}$$

$$u^\epsilon(a,t) = u^\epsilon(b,t), \quad u_x^\epsilon(a,t) = u_x^\epsilon(b,t), \ \ t > 0. \tag{163}$$

The detailed second-order LSTS method from time t_m to t_{m+1} can be written as

$$u^{\epsilon,*} = \exp(-\mathrm{i}V(x)\Delta t/2\epsilon)u^{\epsilon,m}, \tag{164}$$

$$u^{\epsilon,**}(x_j) = \sum_{k=-M}^{M} K_{h,\mathrm{r}}\left(kh, \frac{1}{2}\Delta t\right) u^{\epsilon,*}(x_j - kh), \tag{165}$$

$$u^{\epsilon,m+1} = \exp(-\mathrm{i}V(x)\Delta t/2\epsilon)u^{\epsilon,m}. \tag{166}$$

For a comparison, we define the Crank–Nicolson LS method (CNLS):

$$\frac{u^{\epsilon,m+1} - u^{\epsilon,m}}{\Delta t} = \frac{\mathrm{i}\epsilon}{4}(D_{xx}u^{\epsilon,m+1} + D_{xx}u^{\epsilon,m}) - \frac{\mathrm{i}V(x)}{2\epsilon}(u^{\epsilon,m+1} + u^{\epsilon,m}), \tag{167}$$

where D_{xx} is the LS differential operator approximating and is defined by Eq. (86). The other two schemes used for the comparison are the Crank–Nicolson finite difference method (CNFD) and the FPTS method.

In our computation, the initial condition is always chosen in the classical WKB form

$$u^\epsilon(\mathbf{x}, t = 0) = u_0^\epsilon(\mathbf{x}) = \sqrt{n_0(\mathbf{x})}\mathrm{e}^{\mathrm{i}S_0(\mathbf{x})/\epsilon}. \tag{168}$$

Example 1. The initial condition is taken as

$$n_0(x) = (\mathrm{e}^{-25(x-0.5)^2})^2, \quad S_0(x) = -\frac{1}{5}\ln\left(\mathrm{e}^{5(x-0.5)} + \mathrm{e}^{-5(x-0.5)}\right), \quad x \in R. \tag{169}$$

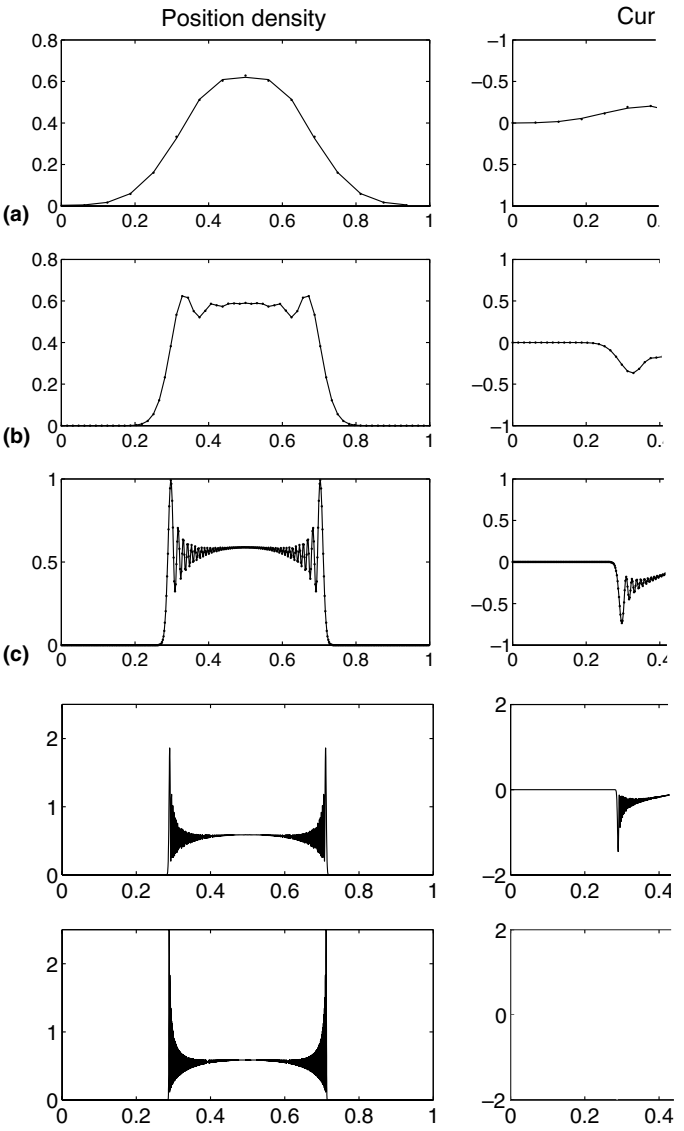
Position density
Cur
(a)
(b)
(c)

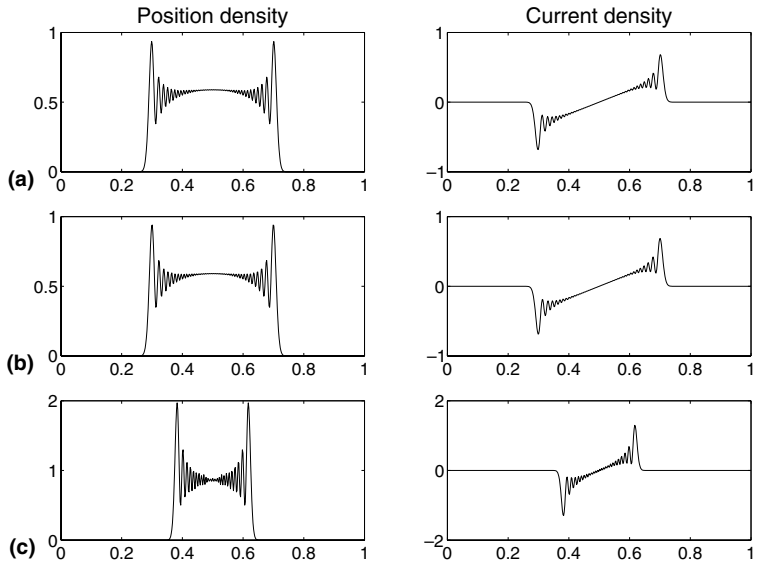

Fig. 26. Numerical solutions at $t = 0.54$ for Example 1 in Section 4.5. $\epsilon = 10^{-3}$, $h = \frac{1}{512}$. (a) LSTS; (b) CNLSP, $\Delta t = 0.00001$; (c) CNLSP, $\Delta t = 0.0001$.

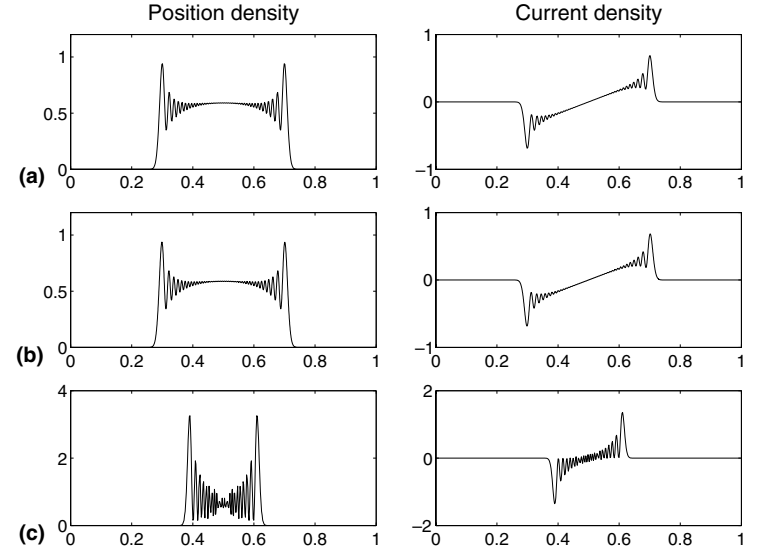

Fig. 27. Numerical solutions at $t = 0.54$ for Example 1 in Section 4.5. $\epsilon = 10^{-3}$, $\Delta t = 0.00001$. (a) CNLS, $h = \frac{1}{512}$; (b) CNFD, $h = \frac{1}{4096}$; (c) CNFD, $h = \frac{1}{512}$.

$$\frac{h}{\epsilon} = \mathrm{O}(1), \tag{170}$$

the numerical solutions convergence (in the weak sense) to the limit solution as $\epsilon \to 0$.

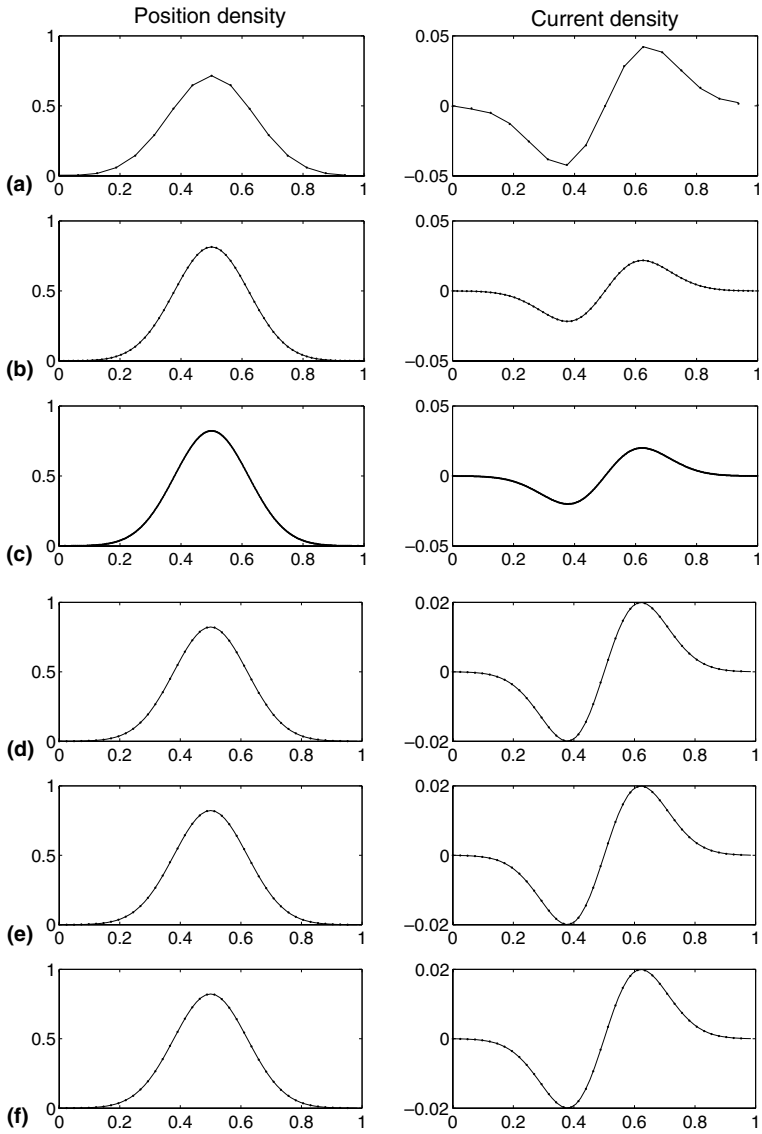

Fig. 28. Numerical solutions at $t = 0.54$ for Example 2 in Section 4.5 by using both the LSTS and the FPTS. (a) $\epsilon = 0.0256, h = \frac{1}{16}$; (b) $\epsilon = 0.0064$, $h = \frac{1}{64}$; (c) $\epsilon = 0.0008, h = \frac{1}{512}$; (d) $\epsilon = 0.0001$, $h = \frac{1}{4096}$; (e) $\epsilon = 0.000025$, $h = \frac{1}{16384}$; (f) $\epsilon = 0.0000125$, $h = \frac{1}{32768}$. Solid lines represent the results by the LSTS. Dots represent the results by the FPTS.

We solve the problem in the interval [0, 1], i.e., $a = 0$ and $b = 1$ with periodic boundary conditions. Let $V(x) = 10$ be a constant potential. The weak limits of Example 1 at $t = 0.54$ are given by Bao et al. [34]. We compute the solution of this problem in one step by the LSTS and FPTS methods because there is no time-discretization error for the constant potential. Fig. 25 shows the numerical solutions at $t = 0.54$ for Example 1 by using both the LSTS and FPTS methods.

In order to show the importance of the time-splitting scheme, we consider the CNLS method. Fig. 26 shows the numerical solutions at $t = 0.54$ in Example 1 when $\epsilon = 0.001$ by both the LSTS and CNLS

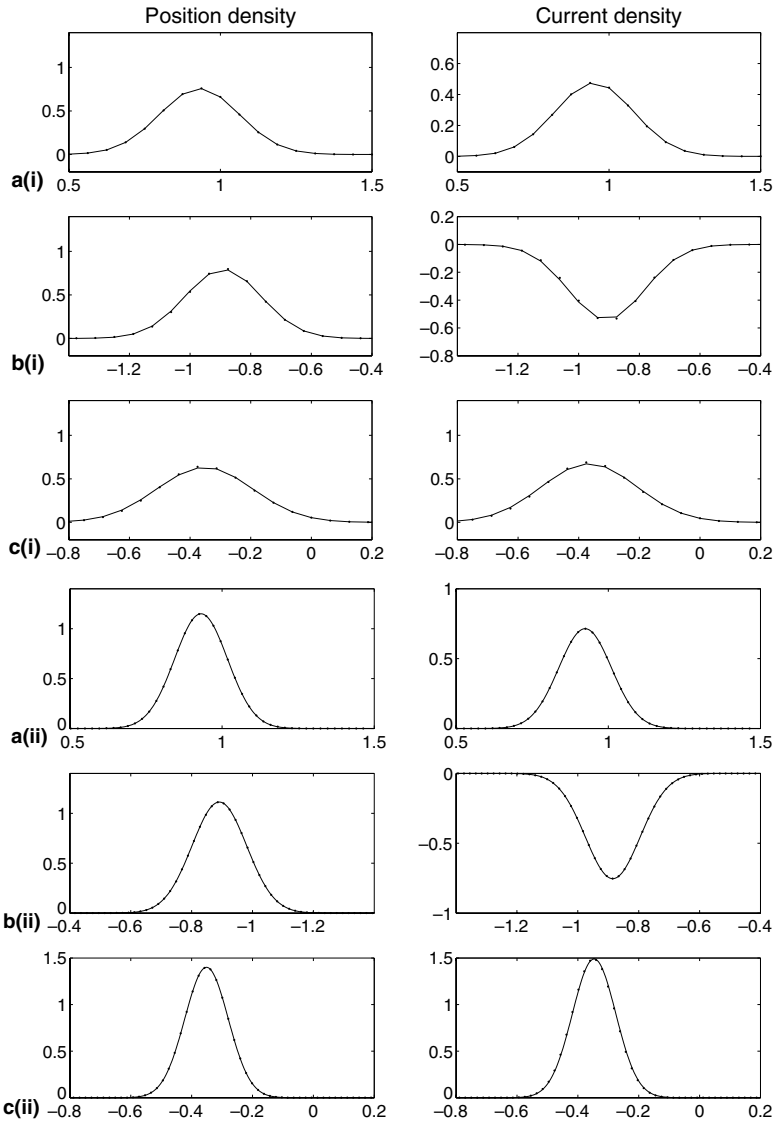

Fig. 29. Numerical solutions at different times for Example 3 in Section 4.5 by using both the LSTS and the FPTS. (a) $t = 0.52$; (b) $t = 3.6$; (c) $t = 5.5$. (i) $\epsilon = 0.04$, $h = \frac{1}{16}$, (ii) $\epsilon = 0.0025$, $h = \frac{1}{256}$, (iii) $\epsilon = 0.00015625$, $h = \frac{1}{4096}$. Solid lines represent the results by the LSTS. Dots represent the results by the FPTS.

methods. The mesh size for both methods is the same, $h = 1/512$. The LSTS method solves the problem in one time step, while the high oscillation of the solution in time takes the CNLS method 54,000 steps to get a comparable result. It is indicated that the correct mesh strategy for CNLS is

$$\frac{h}{\epsilon} = \mathrm{O}(1), \quad \frac{\Delta t}{\epsilon} = \mathrm{o}(1). \tag{171}$$

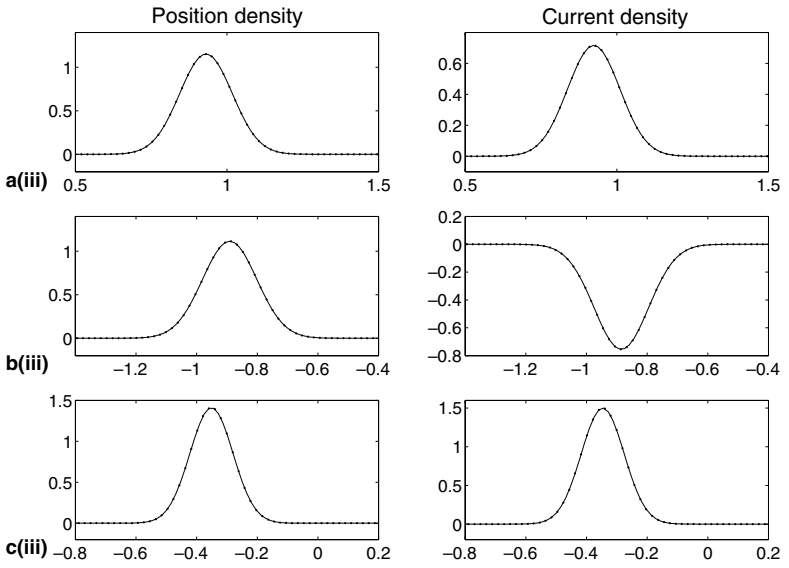

Fig. 29 (*continued*)

The LSTS method shows great advantage in this case because it solves this system analytically. Therefore, even the solution of this system highly oscillates in time, the step size of the LSTS method can be arbitrarily large.

We then compare the difference between the LS and finite difference discretizations. A very small step size Δt is chosen for both CNLS and CNFD methods to significantly reduce temporal discretization errors. Fig. 27 shows the numerical solution of these two methods at $t = 0.54$ for different mesh size h. As one can see, the CNFD method requires a much smaller mesh size than the CNLS method does to attain a similar result. It is indicated that the mesh strategy for the CNFD method should be

$$\frac{h}{\epsilon} = o(1), \quad \frac{\Delta t}{\epsilon} = o(1). \tag{172}$$

Example 2. The initial condition is taken as

$$n_0(x) = (e^{-25(x-0.5)^2})^2, \quad S_0(x) = 0.2(x^2 - x). \tag{173}$$

Let $V(x) = 100$ be the constant potential. The weak limit of Example 2 at $t = 0.54$ is given in Ref. [34]. Fig. 28 shows the numerical solution by both the LSTS and FPTS methods at $t = 0.54$ for Example 2 with different combinations of ϵ,h. A similar conclusion can be drawn as in Example 1.

In the next example, we perform tests on the LSTS for inhomogeneous potentials.

Example 3. The initial condition is taken as

$$n_0(x) = (e^{-25(x-0.5)^2})^2, \quad S_0(x) = x + 1. \tag{174}$$

Let $V(x) = x^2/2$. The weak limit is given in [34]. We solve the problem in the interval $[-2, 2]$ with periodic boundary conditions. Fig. 29 shows the numerical solutions at $t = 0.52$, $t = 3.6$ and $t = 5.5$ by both the LSTS and FPTS methods with $\Delta t = 0.02$ and (i) $\epsilon = 0.04$, $h = \frac{1}{16}$, (ii) $\epsilon = 0.0025$, $h = \frac{1}{256}$, (iii) $\epsilon = 0.00015625$, $h = \frac{1}{4096}$. The numerical solutions converge (in the weak sense) to the weak limit as $\epsilon \to 0$.

5. Conclusions

This paper proposes a local spectral time-splitting (LSTS) method for solving partial differential equations. The LSTS method is developed by combining a local spectral evolution kernel (LSEK) with standard high-order time-splitting methods. The LSEK is derived from the Hermite function expansion of a time evolution operator. The spectral accuracy of the proposed local spectral method is validated by extensive experiments in one- and two-spatial dimensions with the Fokker–Planck equation, the heat equation, the linear and nonlinear Schrödinger equations. The frequency responses of the LSEK are analyzed by the discrete Fourier transform and the parameter dependence of the LSEK is investigated by simulating traveling

Table 16
Nomenclature

$A(t)$	Coefficients of the second-order derivative
$B(t)$	Coefficients of the first-order derivative
$C(t)$	Coefficients of the function
$A^t_{t'}, B^t_{t'}, C^t_{t'}$	$X^t_{t'} = \int_{t'}^{t} X(s)\,\mathrm{d}s$, $X = A, B, C$
$\|f\rangle$	Dirac notation, ket vector
$\langle f\|$	Dirac notation, bra vector
$\langle f\|g\rangle$	Inner product, $\langle f\|g\rangle = \int f^*(x)g(x)\mathrm{d}x$
$\langle x\|f\rangle$	$\langle x\|f\rangle = f(x)$, the position representation of vector $\|f\rangle$
$H_n(x)$	Hermite polynomials
h	The grid spacing
$h_n(x)$	Hermite function, $h_n(x) = \exp(-x^2)H_n(x)$
$K(x,x',t,t')$	Evolution operator
$K_{h,\mathsf{r}}(x,t,t')$	Local spectral evolution kernel
$\hat{K}_{h,\mathsf{r}}(\mathsf{x})$	The Fourier transform of the LSEK
k	Wave number
$\mathbf{k}$	Wave number operator
$L^\infty(R)$	The L^∞ norm space
L_∞	Maximum absolute error measure
$L^2(R)$	The Hilbert space
L_2	Root mean squared error measure
l[int]	The lth derivative
M[int]	The width of the stencils on one side
M_h[int]	The highest degree of the Hermite function
n[int]	The degree of the Hermite function
N[int]	The total number of grid points
r	The ratio of r and h, $r = \mathsf{r}/h$
X_x, X_y	Self-evident quantities in 2D, $X = M, K, h, \mathsf{r}, N$
Z^+	The set of all positive integers
Δt	Time step
$\mathsf{d}(x)$	The delta distribution
$\mathsf{d}_{h,\mathsf{d}}(x)$	DSC kernels
k	Wave length
x	Angular frequence
r	The width of the Gaussian regularizer

Table 17
Abbreviation

ASD	Accurate space derivative (method)
BECs	Bose–Einstein condensates
CFL	The Courant–Friedrich–Lewy (constraint)
CNFD	Crank–Nicolson finite difference (method)
CNLS	Crank–Nicolson local spectral (method)
DSC	Discrete singular convolution (method)
DSC-RK4	Discrete sigular convolution with fourth-order Runge–Kutta
FP	Fourier pseudospectral (method)
FP-RK4	Fourier pseudospectral with fourth-order Runge–Kutta
FPTS	Fourier pseudospectral time splitting (method)
FFT	Fast Fourier transform
GPE	Gross–Pitaevskii equation
KdV	The Korteweg–de Vries equation
LS	Local spectral (method)
LSEK	Local spectral evolution kernel
LSTS	Local spectral time splitting (method)
NLS	The nonlinear Schrödinger equation
PPW	Points per wavelength
TS	Time-splitting (method)
ZS	The Zakharov system

plane waves. The computing time and efficiency of the LSTS method are compared with those of the Fourier pseudospectral time splitting (FPTS) method in solving the Zakharov system. The high-order LSTS methods are validated by the exact solution of linear harmonic oscillator. The proposed method is applied to the generalized nonlinear Schrödinger equation to further verify its robustness. The LSTS method is employed to solve the ground state and time evolution of the Bose–Einstein condensation. Numerical results in these applied problems further demonstrate the efficiency of the LSTS method. Finally, the LSTS simulations are carried out for the Schrödinger equations in the semi-classical regime, which is a severe test for many other existing methods. Excellent consistence is obtained with the results available in the literature.

In summary, the proposed LSTS method has the following features:

- The LSTS is an explicit, weaker stability constraint, time reversible method. It is unconditionally stable for many problems whose two split parts are both analytically integrable. The LSEK adopts a uniform grid mesh. For a given problem, one just needs to compute the weights of the LSEK once for the whole computation.
- As a local spectral method, the LSTS offers controllable accuracy in both spatial and temporal discretizations. It can be of spectral accuracy in space and arbitrarily high-order accuracy in time, if these are desirable for the problem under study. By simply adopting high degree Hermite polynomials, the LSTS method can deal with highly oscillatory problems, i.e., high frequency problems.
- The complexity of the LSTS method is $(2M + 1)N$ and scales as $O(N)$ at a fixed level of accuracy. Therefore, the LSTS is usually faster than the FPTS. However, under the periodic boundary condition and operating at the spectral level of accuracy for highly oscillatory problems, the LSTS requires slightly more CPU time (about 20%) than the FPTS does for a small N. Nevertheless, asymptotically, the LSTS method requires less CPU time than the FPTS method does as the complexity of the latter scales as $O(N\log N)$.
- As a local spectral method, the LSTS has the same flexibility as finite difference methods in handling complex boundary conditions. It is a method of choice whenever the FPTS does not apply due to the boundary condition.

- The LSTS serves as a good alternative to the FPTS method because of its flexibility in choosing grid points and handling boundary conditions.

Acknowledgements

This work was supported by an NSF Grant IIS-0430987 and by an IRGP grant 71-4834. The authors thank the anonymous reviewers for useful suggestions.

Appendix A

See Table 16 and 17.

References

[1] N.N. Yanenko, The Method of Fractional Steps. The Solution of Problems of Mathematical Physics in Several Variables, Springer, New York, 1971.
[2] W.F. Ames, Numerical Methods for Partial Differential Equations, second ed., Academic Press, New York, 1977.
[3] G.I. Marchuk, Splitting and alternating direction methods, Handbook of Numerical Analysis, vol. I, North-Holland, Amsterdam, 1990, pp. 197–462.
[4] R.S. Verga, Matrix Iterative Analysis, Prentice-Hall, Englewood Cliffs, NJ, 1962.
[5] L. Demkowicz, T.J. Oden, W. Rachowicz, A new finite element method for solving compressible Navier–Stokes equations based on an operator splitting method and h–p adaptivity, Comput. Methods Appl. Mech. Engng. 84 (1990) 275–326.
[6] J.B. Perot, An analysis of the fractional step method, J. Comput. Phys. 108 (1993) 51–58.
[7] R.J. LeVeque, Intermediate boundary conditions for time split methods applied to hyperbolic partial differential equations, Math. Comput. 47 (1986) 37–54.
[8] K.O. Aiyesimoju, R.J. Sobey, Process splitting of the boundary conditions for the advection–dispersion equation, Int. J. Numer. Methods Fluids 9 (1989) 235–244.
[9] L.A. Khan, P.L.-F. Liu, Numerical analyses of operator-splitting algorithms for the two-dimensional advection-diffusion equation, Comput. Meth. Appl. Mech. Engng. 152 (1998) 337–359.
[10] B. Sportisse, An analysis of operator splitting techniques in the stiff case, J. Comput. Phys. 161 (2000) 140–168.
[11] S. Descombes, M. Massot, Operator splitting for nonlinear reaction–diffusion systems with an entropic structure: singular perturbation and order reduction, Numer. Math. 97 (2004) 667–698.
[12] G. Strang, On the construction and comparison of difference schemes, SIAM J. Numer. Anal. 5 (1968) 506–517.
[13] D. Goldman, T.J. Kaper, *N*th-order operator splitting schemes and nonreversible systems, SIAM J. Numer. Anal. 33 (1996) 349–367.
[14] B. Gladman, M. Duncan, J. Candy, Symplectic integrators for long-term integrations in celestial mechanics, Celest. Mech. Dyn. Astro. 52 (1991) 221–240.
[15] E. Forest, R.D. Ruth, Fourth order symplectic integration, Physica D 43 (1990) 105–117.
[16] H. Yoshida, Construction of higher order symplectic integrators, Phys. Lett. A 150 (1990) 262–268.
[17] J. Laskar, P. Robutel, High order symplectic integrators for perturbed Hamiltonian systems, Celestial Mech. Dynam. Astr. 80 (2001) 39–62.
[18] B.M. Herbst, M.J. Ablowitz, Numerically induced chaos in the nonlinear Schrödinger equation, Phys. Rev. Lett. 62 (1989) 2065–2068.
[19] M.J. Ablowitz, B.M. Herbst, C. Schober, On the numerical solution of the sine-Gordon equation. 1. Integrable discretizations and homoclinic manifolds, J. Comput. Phys. 126 (1996) 299–314.
[20] G.W. Wei, Discrete singular convolution for the sine-Gordon equation, Physica D 137 (2000) 247–259.
[21] R.H. Hardin, F.D. Tappert, Applications of the split-step Fourier method to the numerical solution of nonlinear and variable coefficient wave equations, SIAM Review 15 (1973) 423.
[22] A. Hasegawa, F. Tappert, Transmission of stationary nonlinear optical pulses in dispersive dielectric fibers. I. Anomalous dispersion, Appl. Phys. Lett. 23 (1973) 142–144.

[23] D. Goldman, L. Sirovich, A novel method for simulating the complex Ginzburg–Landau equation, Quart. Appl. Math. 53 (1995) 315–333.
[24] B. Fornberg, T.A. Driscoll, A fast spectral algorithm for nonlinear wave equations with linear dispersion, J. Comput. Phys. 155 (1999) 456–467.
[25] T.R. Taha, M.J. Ablowitz, Analytical and numerical aspects of certain nonlinear evolution equations, II. Numerical, nonlinear Schrödinger equation, J. Comput. Phys. 55 (1984) 203–230.
[26] T.R. Taha, M.J. Ablowitz, Analytical and numerical aspects of certain nonlinear evolution equations, III. Numerical, Korteweg–de Vries equation, J. Comput. Phys. 55 (1984) 231–253.
[27] H. Holden, K.H. Karlsen, N.H. Risebro, Operator splitting methods for generalized Korteweg–de Vries equations, J. Comput. Phys. 153 (1999) 203–222.
[28] G.M. Muslu, H.A. Erbay, A split-step Fourier method for the complex modified Korteweg–de Vries equation, Comput. Math. Appl. 45 (2003) 503–514.
[29] J. Lee, B. Fornberg, A split step approach for the 3-D Maxwell's equations, J. Comput. Appl. Math. 158 (2003) 485–505.
[30] G.S. Jiang, C.W. Shu, Efficient implementation of weighted ENO schemes, J. Comput. Phys. 126 (2003) 202–228.
[31] S. Jin, P.A. Markowich, C. Zheng, Numerical simulation of a generalized Zakharov system, J. Comput. Phys. 201 (2004) 376–395.
[32] W. Bao, J. Shen, A Fourth-order time-splitting Laguerre–Hermite pseudo-spectral method for Bose–Einstein condensates, SIAM J. Sci. Comput. in press (2005).
[33] W. Bao, Q. Du, Computing the ground state solution of Bose–Einstein condensates by a normalized gradient flow, SIAM J. Sci. Comput. 25 (2004) 1674–1697.
[34] W. Bao, S. Jin, P.A. Markowich, On time-splitting spectral approximation for the Schrödinger equation in the semiclassical regime, J. Comput. Phys. 175 (2002) 487–524.
[35] P. Lazaridis, G. Debarge, P. Gallion, Split-step-Gauss–Hermite algorithm for fast and accurate simulation of soliton propagation, Int. J. Numer. Model. Elect. Netw. Dev. Fields 14 (2001) 325–329.
[36] T. Kremp, A. Killi, A. Rieder, W. Freude, Split-step wavelet collocation method for nonlinear optical pulse propagation, IEICE Trans. Electron. 3 (2002) 534–543.
[37] D. Gottlieb, S.A. Orszag, Numerical Analysis of Spectral Methods: Theory and Applications, Society for Industrial and Applied Mathematics, Philadelphia, 1977.
[38] D. Gottlieb, The stability of pseudospectral-Chebyshev methods, Math. Comput. 36 (1981) 107–118.
[39] D. Gottlieb, S.A. Orszag, E. Turkel, Stability of pseudospectral and finite-difference methods for variable coefficient problems, Math. Comput. 37 (1981) 293–305.
[40] W. Cai, D. Gottlieb, C.W. Shu, Essentially nonoscillatory spectral Fourier methods for shock wave calculations, Math. Comput. 52 (1989) 389–410.
[41] D. Gottlieb, E. Tadmor, The CFL condition for spectral approximations to hyperbolic initial-boundary value problems, Math. Comput. 56 (1991) 565–588.
[42] D. Gottlieb, J.S. Hesthaven, Spectral methods for hyperbolic problems, J. Comput. Appl. Math. 128 (2001) 83–131.
[43] W.S. Don, D. Gottlieb, J.H. Jung, A multidomain spectral method for supersonic reactive flows, J. Comput. Phys. 192 (2003) 325–354.
[44] C. Canuto, Y. Hussaini, A. Quarteroni, T. Zang, Spectral Methods in Fluid Dynamics, Springer, New York, 1988.
[45] J.P. Boyd, Chebyshev and Fourier Spectral Methods, Springer, 1989.
[46] B. Fornberg, A Practical Guide to Pseudospectral Methods, Cambridge University Press, 1996.
[47] L.N. Trefethen, Spectral Methods in Matlab, SIAM, Philadelphia, 2000.
[48] Ying Wang, Y.B. Zhao, G.W. Wei, A note on the numerical solution of high-order differential equations, J. Comput. Appl. Math. 159 (2003) 387–398.
[49] A.T. Patera, A spectral element method for fluid dynamics – laminar flow in a channel expansion, J. Comput. Phys. 54 (1984) 468–488.
[50] G.E. Karniadakis, M. Iseraeli, S.A. Orszag, High order splitting methods for the incompressible Navier–Stokes equations, J. Comput. Phys. 97 (1991) 414–443.
[51] G.W. Wei, Discrete singular convolution for the Fokker–Planck equation, J. Chem. Phys. 110 (1999) 8930–8942.
[52] G.W. Wei, Y.B. Zhao, Y. Xiang, Discrete singular convolution and its application to the analysis of plates with internal supports. I. Theory and algorithm, Int. J. Numer. Methods Engng. 55 (2002) 913–946.
[53] G.W. Wei, A unified approach for the solution of the Fokker–Planck equation, J. Phys. A, Math. General 33 (2000) 4935–4953.
[54] S. Zhao, G.W. Wei, Comparison of the discrete singular convolution and three other numerical schemes for Fisher's equation, SIAM J. Sci. Comput. 25 (2003) 127–147.
[55] G.W. Wei, Vibration analysis by discrete singular convolution, J. Sound Vibr. 244 (2001) 535–553.
[56] G.W. Wei, A new algorithm for solving some mechanical problems, Comput. Methods Appl. Mech. Engng. 190 (2001) 2017–2030.

[57] S. Zhao, G.W. Wei, Y. Xiang, DSC analysis of free-edged beams by an iteratively matched boundary method, J. Sound Vib., in press (2005).
[58] D.C. Wan, B.S.V. Patnaik, G.W. Wei, Discrete singular convolution-finite subdomain method for the solution of incompressible viscous flows, J. Comput. Phys. 180 (2002) 229–255.
[59] Y.C. Zhou, G.W. Wei, High-resolution conjugate filters for the simulation of flows, J. Comput. Phys. 189 (2003) 150–179.
[60] Y.C. Zhou, B.S.V. Patnaik, D.C. Wan, G.W. Wei, DSC solution for flow in a staggered double lid driven cavity, Int. J. Numer. Meth. Engng. 57 (2003) 211–234.
[61] G. Bao, G.W. Wei, S. Zhao, Numerical solution of the Helmholtz equation with high wave numbers, Int. J. Numer. Meth. Engng. 59 (2004) 389–408.
[62] Z.H. Shao, G.W. Wei, S. Zhao, DSC time-domain solution of Maxwell's equations, J. Comput. Phys. 189 (2003) 427–453.
[63] G. Bao, G.W. Wei, S. Zhao, Local spectral time-domain method for electromagnetic wave propagation, Opt. Lett. 28 (2003) 513–515.
[64] Z.J. Hou, G.W. Wei, A new approach for edge detection, Pattern Recogn. 35 (2002) 1559–1570.
[65] G.W. Wei, Y.B. Zhao, Y. Xiang, A novel approach for the analysis of high frequency vibrations, J. Sound Vib. 257 (2002) 207–246.
[66] Y.B. Zhao, G.W. Wei, Y. Xiang, Discrete singular convolution for the prediction of high frequency vibration of plates, Int. J. Solids Struct. 39 (2002) 65–88.
[67] W. Bao, F. Sun, G.W. Wei, Numerical methods for the generalized Zakharov system, J. Comput. Phys. 190 (2003) 201–228.
[68] L.W. Qian, On the regularized Whittaker–Kotel'nikov–Shannon sampling formula, Proc. Amer. Math. Soc. 131 (2003) 1169–1176.
[69] S.Y. Yang, Y.C. Zhou, G.W. Wei, Comparison of the discrete singular convolution algorithm and the Fourier pseudospectral methods for solving partial differential equations, Comput. Phys. Commun. 143 (2002) 113–135.
[70] J. Korevaar, Mathematical Methods, vol. 1, Academic Press, New York, 1968.
[71] G.G. Walter, J. Blum, Probability density estimation using delta sequences, Ann. Statist. 7 (1977) 328–340.
[72] G.W. Wei, D.S. Zhang, D.J. Kouri, D.K. Hoffman, Lagrange distributed approximating functionals, Phys. Rev. Lett. 79 (1997) 775–778.
[73] J. Korevaar, Pansions and the theory of Fourier transforms, Amer. Math. Soc. Trans. 91 (1959) 53–101.
[74] D.K. Hoffman, N. Nayar, O.A. Sharafeddin, D.J. Kouri, Analytic banded approximation for the discretized free propagator, J. Phys. Chem. 95 (1991) 8299–8305.
[75] G.W. Wei, D.S. Zhang, D.J. Kouri, D.K. Hoffman, Distributed approximating functional approach to the Fokker–Planck equation: Time propagation, J. Chem. Phys. 107 (1997) 3239–3246.
[76] G.W. Wei, H. Wang, D.J. Kouri, M. Papadakis, I.A. Kakadiaris, D.K. Hoffman, On the mathematical properties of distributed approximating functionals, J. Math. Chem. 30 (2001) 83–107.
[77] R.L. Liboff, Introductory Quantum Mechanics, Addison-Wesley, 1998.
[78] M.F. Wehner, W.G. Wolfer, Numerical evaluation of path-integral solutions to Fokker–Planck equations, Phys. Rev. A 27 (1983) 2663–2670.
[79] F. Black, M.S. Scholes, The pricing of options and corporate liabilities, J. Polit. Econ. 81 (1973) 637–654.
[80] Y.K. Kwok, Mathematical Models of Financial Derivatives, Springer, Berlin, 1998.
[81] P. Boyle, M. Broadie, P. Glasserman, Monte Carlo methods for security pricing, J. Econ. Dynam. Control 21 (1997) 1267–1321.
[82] M.J. Brennan, E.S. Schwartz, Finite-difference methods and jump processes arising in the pricing of contingent claims: a synthesis, J. Financ. Quant. Anal. 13 (1978) 461–474.
[83] Y. Tian, A modified lattice approach to option pricing, J. Futures Markets 13 (1993) 563–577.
[84] R.A. Fisher, The wave of advantage of advantageous genes, Ann. Eugenics 7 (1937) 355–369.
[85] A. Kolmogorov, I. Petrovshy, N. Piscounoff, Étude de l'équation de la diffusion aveccroissance de la quanitité de matière et son application à un problème biologique, Bull. Univ. Etat Moscou Ser. Int. Sect. A Math. et Mecan. 1 (1937) 1–25.
[86] J. Canosa, On a nonlinear diffusion equation describing population growth, IBM J. Res. Develop. 17 (1973) 307–313.
[87] D.A. Larson, Transient bounds and time-asymptotic behavior of solutions to nonlinear equations of Fisher type, SIAM J. Appl. Math. 34 (1978) 93–103.
[88] P.S. Hagan, Traveling wave and multiple traveling wave solutions of parabolic equations, SIAM J. Math. Anal. 13 (1982) 717–738.
[89] T. Hagstrom, H.B. Keller, The numerical calculation of traveling wave solutions of nonlinear parabolic equations, SIAM J. Sci. Stat. Comput. 7 (1986) 978–988.
[90] J. Gazdag, J. Canosa, Numerical solution of Fisher's equation, J. Appl. Probab. 11 (1974) 445–457.
[91] G.F. Carey, Y. Shen, Least-squares finite element approximation of Fisher's reaction diffusion equation, Numer. Meth. Partial Differential Equations 11 (1995) 175–186.
[92] S. Li, L.R. Petzold, Y. Ren, Stability of moving mesh systems of partial differential equations, SIAM J. Sci. Comput. 20 (1998) 719–738.

[93] T. Mavoungou, Y. Cherruault, Numerical study of Fisher's equation by Adomian's method, Math. Comput. Model. 19 (1994) 89–95.
[94] I. Blalynickl-Birdla, J. Mycielski, Gaussons: solutions of the logarithmic Schrödinger equations, Sci. Sinica Ser. A 26 (1983) 687.
[95] R.T. Bullough, P.M. Jack, P.W. Kitchenside, R. Saunders, Solutions in laser physics, Phys. Scripta 20 (1979) 364–381.
[96] D. Pathria, J.L. Morris, Pseudo-spectral solution of nonlinear Schrödinger equations, J. Comput. Phys. 87 (1990) 108–125.
[97] Q. Chang, E. Jia, W. Sun, Difference schemes for solving the generalized nonlinear Schrödinger equation, J. Comput. Phys. 148 (1999) 397–415.
[98] L. Landau, E. Lifschitz, Quantum Mechanics: Non-relativistic Theory, Pergamon Press, New York, 1977.
[99] L.P. Pitaevskii, Vortex lines in an imperfect Bose gas, Sov. Phys. JETP 13 (1961) 451–454.
[100] J.R. Anglin, W. Ketterle, Bose–Einstein condensation of atomic gases, Nature 416 (2002) 211–218.
[101] E. Cornell, Very cold indeed: The nanokelvin physics of Bose–Einstein condensation, J. Res. Natl. Inst. Stan. 101 (1996) 419–434.
[102] F. Dalfovo, S. Giorgini, L.P. Pitaevskii, S. Stringari, Theory of Bose–Einstein condensation in trapped gases, Rev. Mod. Phys. 71 (1999) 463–512.
[103] S.K. Adhikari, Numerical solution of the two-dimensional Gross–Pitaevskii equation for trapped interacting atoms, Phys. Lett. A 265 (2000) 91–96.
[104] M.L. Chiofalo, S. Succi, M.P. Tosi, Ground state of trapped interacting Bose–Einstein condensates by an explicit imaginary-time algorithm, Phys. Rev. E 62 (2000) 7438–7444.
[105] E.H. Lieb, R. Seiringer, J. Yngvason, Bosons in a trap: a rigorous derivation of the Gross–Pitaevski energy functional, Phys. Rev. A 61 (2000) 043602.
[106] M.M. Cerimele, M.L. Chiofalo, F. Pistella, S. Succi, M.P. Tosi, Numerical solution of the Gross–Pitaevskii equation using an explicit finite-difference scheme: an application to trapped Bose–Einstein condensates, Phys. Rev. E 62 (2000) 1382–1389.
[107] Q. Du, Numerical computations of quantized vortices in Bose–Einstein condensate, in: T. Chan, et al. (Eds.), Recent Progress in Computational and Applied PDEs, Kluwer Academic, Dordrecht, The Netherlands, 2002, p. 155.
[108] P.A. Markowich, P. Pietra, C. Pohl, Numerical approximation of quadratic obsevables of Schrödinger-type equations in the semi-classical limit, Numer. Math. 81 (1999) 595–630.